

Calibration and Image Reconstruction Techniques for FMCW MIMO Radars with Consideration of Antenna Radiation Patterns

Kalibrations- und Bildrekonstruktionsverfahren für FMCW-MIMO-Radare
unter Berücksichtigung der Antennenabstrahlungscharakteristik

Daniel Gotzens

Masterarbeit vorgelegt dem

 **IHF** Institut für
Hochfrequenz-
technik |  **RWTHAACHEN**
UNIVERSITY
Lehrstuhl für Radarsystemtechnik
Institut für Hochfrequenztechnik
RWTH Aachen University
March 4, 2024

In Kooperation mit

indurad GmbH Aachen

Contents

Chapter 1. Introduction	3
1. Radar Applications in Mining	3
2. MIMO Radar Sensors	4
3. Imaging Algorithms for 3D MIMO Radar Sensors	4
4. Thesis Outline	5
Chapter 2. Radar Fundamentals: Theoretical Background	7
1. Antenna Fundamentals	7
1.1. Physical Background	7
1.2. Antenna Parameters	7
1.3. Antenna Arrays	9
2. Signal Model	9
2.1. Single Channel FMCW	9
2.2. Multiplexing Techniques	11
2.3. Multi-Channel FMCW	11
2.4. Discrete Fourier Transform	12
2.5. Virtual Antenna Arrays	12
3. Image Reconstruction	13
3.1. FFT-based Imaging	13
3.2. Backprojection Imaging	14
3.3. MUSIC Imaging	15
3.4. Complexity Analysis	16
Chapter 3. Hardware Evaluation	17
1. Indurad Multi-Channel Radar	17
1.1. System Parameters	17
1.2. Virtual Antenna Array	19
2. Stability Analysis	21
2.1. Setup	21
2.2. Preprocessing and Analysis	22
2.3. Effects of System Temperature and Runtime	23
2.4. Differences between Antennas	23
2.5. Effects of Self-Calibration	24
2.6. Conclusion	24
3. Antenna Characteristics	27
3.1. Experiment Setup	27
3.2. Preprocessing and Analysis	27
3.3. Range Estimation	28
3.4. Amplitude	30
3.5. Phase Estimation Techniques	31
3.6. Phase Analysis	35
3.7. Antenna Separation	35
3.8. Conclusion	38

Chapter 4. Image Reconstruction	41
1. PyTorch	41
2. FFT-Based Imaging	41
2.1. Direction of Arrival Accuracy	42
2.2. Offline Calibration	45
2.3. Test Image	45
3. Backprojection Imaging	45
3.1. Direction of Arrival Accuracy	47
3.2. Test Image	49
4. Hybrid Approach	50
4.1. Direction of Arrival Accuracy	50
4.2. Test Image	50
5. Conclusion	51
Chapter 5. Conclusion and Discussion	55
1. Overview	55
2. Key Findings	56
3. Outlook and Discussion	56
Appendix A. Bibliography	59
Appendix B. Code	61
1. Introduction to PyTorch Sensor Processing	61
2. Listings	63
Appendix C. Additional Experiments	67
List of Figures	69
List of Tables	71

CHAPTER 1

Introduction

Radar technology has undergone significant advancements over the decades, revolutionizing various fields including aerospace, defense, automotive, and healthcare. Its fundamental principle of using electromagnetic waves to detect the presence, direction, distance, and speed of objects has enabled myriad applications, ranging from weather monitoring to target tracking.

Within this expansive domain, Frequency Modulated Continuous Wave (FMCW) Multiple Input Multiple Output (MIMO) Millimeter Wave (mmWave) radar systems have emerged as a cutting-edge solution with unparalleled capabilities. FMCW radar, characterized by its continuous transmission of frequency-modulated signals, combined with MIMO architecture, which utilizes multiple antennas for both transmission and reception, has enabled enhanced spatial resolution, improved target detection, and increased resilience to interference. Operating in the mmWave spectrum, typically within the frequency range of 24 to 100 GHz, these radars offer advantages such as high resolution, immunity to environmental conditions like fog and precipitation, and the ability to accommodate large bandwidths for high data rates.

The fusion of FMCW, MIMO, and mmWave technologies represents a significant leap forward in radar sensing, promising to address the evolving demands of modern applications ranging from autonomous vehicles to biomedical imaging. This thesis endeavors to contribute to this dynamic field by proposing and evaluating novel imaging algorithms optimized for FMCW MIMO mmWave radar systems, with a focus on enhancing their performance, efficiency, and applicability across diverse scenarios and applications.

1. Radar Applications in Mining

Radar technology finds diverse applications across various industries, with one notable area being mining. In the mining sector, radar systems play a crucial role in enhancing safety, efficiency, and productivity.

Radar-based collision avoidance systems are employed in mining operations to prevent accidents involving heavy machinery and personnel. These systems utilize radar sensors to detect nearby objects and provide real-time alerts to operators, facilitating safe maneuvering in challenging environments.

Moreover, radar technology is instrumental in various logistical aspects of mining operations. It is utilized for stockpile management, enabling accurate measurement and monitoring of ore and waste material reserves, optimizing inventory control and resource allocation. Radar sensors are also integrated into silo and train loading processes, ensuring efficient and precise transfer of bulk materials onto transport vehicles. Furthermore, radar-based systems facilitate ship unloading and berthing operations at port facilities, streamlining the handling of bulk commodities. One significant advantage of radar systems over visual-based solutions in mining environments is their resilience to omnipresent dust and grime. Unlike optical systems, radar sensors are not affected by adverse weather conditions or

obstructed visibility, ensuring reliable performance and continuous operation even in harsh mining environments.

2. MIMO Radar Sensors

In the realm of radar sensing, various approaches exist for achieving multidimensionality in imaging. Traditional radar systems employ one-dimensional (1D) sensors, which provide information along a single axis, typically range. These sensors are adept at measuring distances to targets but lack detailed spatial information. To overcome this limitation, two-dimensional (2D) sensors have been developed, capable of scanning in both range and azimuth dimensions, providing a more comprehensive view of the surrounding environment. These sensors often achieve multidimensionality either mechanically, by utilizing mechanisms such as rotating antennas or electronically with phased arrays to sweep the radar beam across the scene. Additionally, three-dimensional (3D) radar sensors offer even greater spatial resolution by adding an elevation dimension to the azimuth and range measurements. These sensors are commonly used in applications requiring detailed volumetric imaging. The mechanical movement or rotation of the sensor enables it to scan the scene from multiple angles, capturing information in three dimensions.

The evolution of radar technology has led to the development of advanced imaging techniques that leverage the principles of Multiple Input Multiple Output (MIMO) radar systems. These systems, characterized by their use of multiple transmit and receive antennas, offer significant improvements in imaging performance compared to traditional radar architectures. One key advantage of MIMO radar is its ability to achieve multidimensional imaging without the need for mechanically rotating antennas. By utilizing multiple antennas in a static configuration, MIMO radar systems can capture spatial information along multiple dimensions simultaneously, leading to enhanced imaging capabilities at reduced cost and complexity. Additionally, MIMO radar systems offer the potential for higher frame rates compared to traditional radar systems. With multiple antennas operating in parallel, MIMO radar can sample the scene more frequently, enabling rapid data acquisition and real-time imaging of dynamic environments. The next step in the advancement of MIMO imaging radars involves the development and optimization of sophisticated signal processing algorithms tailored to exploit the full potential of these systems. These algorithms aim to extract rich spatial information from the received signals, enabling high-fidelity imaging of complex scenes with unprecedented detail and accuracy.

3. Imaging Algorithms for 3D MIMO Radar Sensors

Current 3D imaging algorithms employed for many FMCW MIMO radars rely on the Fast Fourier Transform (FFT) technique for generating three-dimensional reconstructions of the observed scene. This algorithm computes each dimension of the image by performing an FFT on a different dimension of the Intermediate Frequency (IF) signal obtained from the radar's input data.

One of the primary strengths of this approach lies in its fast implementation, allowing for rapid processing of radar data. However, despite its efficiency, the FFT-based algorithm suffers from several limitations.

These include near-field distortion issues, restrictions in applicability to Uniform Linear Arrays (ULA), the necessity for array calibration, and the inability

to utilize measured antenna gains effectively. Moreover, the algorithm is prone to ringing artifacts, which can degrade the quality of reconstructed images, particularly in complex or cluttered environments.

In response to the limitations of the current FFT-based approach, a novel back projection algorithm is proposed for 3D imaging in the FMCW MIMO radar system. Unlike the FFT-based method, the proposed algorithm offers increased flexibility and versatility in image reconstruction. One of its key advantages is the elimination of ringing artifacts, which commonly plague FFT-based reconstructions. Additionally, the back projection algorithm is capable of addressing near-field distortion issues and is suitable for both near- and far-field imaging scenarios. Moreover, it exhibits compatibility with non-ULA arrays, enabling broader applicability across different radar configurations. A notable feature of the proposed algorithm is its ability to incorporate measured antenna gains effectively, leading to more accurate and reliable imaging results. By leveraging these advantages, the back projection algorithm promises to significantly enhance the imaging capabilities of the FMCW MIMO radar, paving the way for improved performance and expanded applications in various domains.

4. Thesis Outline

In this thesis, we embark on a comprehensive exploration of advanced imaging techniques for FMCW MIMO radar systems, aiming to address existing challenges and enhance imaging performance.

Chapter 1 provides a thorough examination of the theoretical background underpinning radar imaging, including signal models and a detailed description of the image reconstruction methods. We delve into the intricacies of both FFT-based and proposed back projection algorithms. Furthermore, a detailed hardware description of the FMCW MIMO radar system under investigation is presented, laying the foundation for subsequent experimental chapters.

Chapter 2 focuses on measurements and validation of hardware stability through extensive static measurements. Through rigorous analysis, we assess the stability of the radar system and measure antenna gains, crucial for accurate imaging.

Chapter 3 shifts the focus to imaging algorithms, detailing the implementation of the back projection algorithm using PyTorch. Additionally, we discuss the interpolation of measured gains and evaluate the performance enhancements achieved through these refinements.

By presenting comprehensive results and analyses, this thesis aims to contribute to the advancement of FMCW MIMO radar imaging technology, with implications for various applications in fields such as remote sensing, autonomous vehicles, and surveillance.

CHAPTER 2

Radar Fundamentals: Theoretical Background

This section provides a foundation for understanding the principles and methodologies underpinning FMCW MIMO radar imaging. We begin by elucidating the signal model employed in FMCW radar systems, elucidating the distinctions between single-channel and MIMO configurations. Subsequently, we delve into the intricacies of image reconstruction techniques, exploring both the Discrete Fourier Transform (DFT) approach and the proposed backprojection algorithm.

1. Antenna Fundamentals

The fundamental working principle of radars is to transmit an electromagnetic wave, receive a reflected version of the same wave, and to estimate the local scenery based on how much the signal has changed between transmission and reception. Antennas are the key building block to enable said transmission and reception. They determine the directional characteristics of signals, influencing radar coverage, resolution, and sensitivity. Therefore, a brief overview of both the physical foundation and the technical description of antennas is given in the following.

1.1. Physical Background. The space surrounding a transmit antenna is typically divided into three distinct regions, based on the antennas maximum overall dimension D and the wavelength λ of the propagating wave:

- *reactive near-field region.* In this region the interaction between the antenna and its surrounding medium takes place. Energy oscillates between being stored in the electromagnetic field in the medium and the electrical charge distribution of the antenna.
- *radiating near-field region.* Starting from a distance of $0.62\sqrt{D^3/\lambda}$ (or $\frac{\lambda}{2\pi}$ unless $D \gg \lambda$), the field is made up predominantly of radiation fields emitted by the antenna. In this region, the angular distribution of the field depends on the distance of the antenna.
- *radiating far-field region.* Above a distance of $d_F = 2D^2/\lambda$, the angular distribution of the field stops depending on the distance of the antenna, rendering them essentially transverse.

The radiating near- and far-field regions are sometimes called Fresnel region and Fraunhofer region, respectively. These terms are based on an optical analogy for antennas focused at infinity.

While notable differences exist among the zones, there are no sudden shifts in the field configurations as one transitions between them.

1.2. Antenna Parameters. In the following, a set of key parameters is defined that are used to describe an antenna's performance. They are adapted from the definitions in [7] and [8]. All quotations in this paragraph, unless stated differently, are from [7]. The equations and definitions of symbols are adapted from chapter 2 of [8].

The *radiation pattern* or *antenna pattern* describes the radiation properties of an antenna as a function of spatial coordinates. According to [7], “[the] quantities

that are most often used to characterize the radiation from an antenna are proportional to or equal to power flux density, radiation intensity, directivity, phase, polarization, and field strength.”

For directive antennas, radiation patterns usually form so-called *lobes*, which are the areas between zero crossings of the pattern. The lobe in the direction of maximum gain is called the *major lobe*, while all others are called *minor lobes*. Minor lobes can be further broken down into *side lobes* and *back lobes*, where the back lobe faces in the exact opposite direction of the main lobe, and *side lobes* usually directly next to it. [Figure asdf shows a qualitative example of a radiation pattern, designating one of each type of lobe].

An important measure of a radiation pattern is its half-power beamwidth (HPBW). It corresponds to the angle between the two points in a radiation pattern’s main lobe that are exactly half the power (-3 dB) below the main lobe’s maximum. Other measures include the quarter-power beamwidth (-6 dB from the peak), and the first-null beamwidth (FNBW) which measures the width of the entire main lobe.

The *radiation power density* is derived from electromagnetic field properties, namely the time average Poynting vector. Assuming time-harmonic electric and magnetic fields with

$$(1) \quad \vec{H}(\vec{r}, t) = \Re\{\underline{\vec{H}}(\vec{r})e^{j\omega t}\} \text{ and}$$

$$(2) \quad \vec{E}(\vec{r}, t) = \Re\{\underline{\vec{E}}(\vec{r})e^{j\omega t}\},$$

the time-average Poynting vector becomes

$$(3) \quad \vec{S}_{avg} = \frac{1}{2} \Re\{\underline{\vec{E}} \times \underline{\vec{H}}^*\}.$$

Under far-field conditions, the “power radiated from an antenna per unit solid angle” can be assumed to be independent of distance. That motivates defining this quantity as the *radiation intensity*. It can be expressed in terms of the radial component of the radiation power density:

$$(4) \quad U = r^2 \hat{e}_r \cdot \vec{S}_{avg},$$

where \hat{e}_r is the unit vector in radial direction.

An idealized example, often used as a theoretical reference, is the isotropic lossless radiator, which transforms all input power P_{in} into a planar spherical wave propagating out. Its radiation power density is simply

$$(5) \quad \vec{S}_0 = \frac{P_{in}}{4\pi r^2} \hat{e}_r,$$

making its radiation intensity

$$(6) \quad U_0 = \frac{P_{in}}{4\pi}.$$

Another important quantity is called the antenna gain. The *absolute gain* refers to the ratio of an antenna’s radiation intensity to that of the isotropic lossless radiator receiving the same input power:

$$(7) \quad G_{abs}(\theta, \phi) = \frac{U(\theta, \phi)}{U_0} = \frac{4\pi}{P_{in}} U(\theta, \phi)$$

The *relative gain* refers to the ratio of an antenna’s radiation intensity to that of another antenna that is not necessarily an isotropic lossless radiator:

$$(8) \quad G_{rel}(\theta, \phi) = \frac{U(\theta, \phi)}{U_{ref}(\theta, \phi)} = \frac{4\pi}{P_{in}} U(\theta, \phi)$$

A gain pattern $G(\theta, \phi)$ can further be subdivided into its maximum G and a function $c(\theta, \phi)$ called its *normalized gain pattern*:

$$(9) \quad G(\theta, \phi) = G \cdot c(\theta, \phi)$$

with

$$G = \max G, g(\theta, \phi) = \frac{G(\theta, \phi)}{G}, |g| \in [0, 1]$$

1.3. Antenna Arrays. The radiation patterns of single antennas are usually rather wide. To make it more narrow, the dimensions of the antenna have to be increased (see [8] p. 283). This can be accomplished by using multiple copies of the same antenna arranged into a structure called an *array*. By constructive and destructive interference between the fields generated by the array's elements, the arrays resulting radiation pattern can be increased in the desired direction and decreased in all others. Beside the radiation pattern of the individual antennas, the geometric makeup of the array is chiefly important to the array's radiation pattern. The array's relative gain, expressed with reference to a single array element, is called the *array factor*.

An important variant is the *uniform linear array (ULA)*, which consists of N “identical elements all of identical magnitude and each with a progressive phase” (see [8] pp. 290f.). The array factor can be expressed as a function of the direction θ , the phase offset between elements $\Delta\varphi$, the distance between elements d and the wavenumber $k = \omega/c$:

$$(10) \quad \text{AF} = \frac{\sin\left(\frac{N}{2}\psi\right)}{\sin\left(\frac{1}{2}\psi\right)} \simeq N \text{sinc}\left(\frac{N}{2}\psi\right) \text{ for } \psi \ll 1$$

$$(11) \quad \text{with } \psi = (kd\cos\theta + \delta\varphi)$$

Note that the array factor has an additional factor of $e^{j\psi(N-1)/2}$ if the reference element is not in the center of the array.

Other array configurations include non-uniform linear arrays as well as planar and circular arrays.

2. Signal Model

Understanding the signal model is fundamental to grasp the operation and capabilities of FMCW MIMO radar systems. In this section, we delve into the intricacies of the signal model, beginning with an exploration of Single Channel Frequency Modulated Continuous Wave (FMCW) radar systems. We clarify the key principles governing their signal generation and processing, laying the groundwork for a comprehensive understanding of radar imaging techniques. Then, we extend our analysis to encompass Multiple Input Multiple Output (MIMO) FMCW radar systems, highlighting the unique characteristics and complexities associated with their signal model.

2.1. Single Channel FMCW. A single channel consists of a transmit antenna and a receive antenna. The continuous wave signal $x_{TX}(t)$ send by the transmit antenna is reflected by an ideal point scatterer at position \vec{r}_S and then received at the receive antenna as $x_{RX}(t)$.

Linear sawtooth frequency modulation is a popular type of FMCW [9]. The signal's frequency is modulated with a sawtooth of period T_{chirp} . Within one period, i.e. $t \in [0, T_{chirp}]$, the electric signal of amplitude A_0 ¹ outputted by the transmitter

¹In later sections, it is often assumed without loss of generality that $A_0 = 1$ to reduce the length of equations.

takes the following shape:

$$(12) \quad x_{TX}(t) = A_0 e^{j(\omega_0 t + \frac{1}{2} \dot{\omega} t^2 + \phi_0)}$$

$$(13)$$

After a propagation delay τ , the signal arrives back at the receiver. The propagation delay can be calculated using the speed of light c_0 , and the locations of the scatterer, the receive antenna and the transmit antenna \vec{r}_S , \vec{r}_{RX} and \vec{r}_{TX} :

$$(14) \quad \tau = \frac{\|\vec{r}_{TX} - \vec{r}_S\| + \|\vec{r}_{RX} - \vec{r}_S\|}{c_0}$$

The ratio of receive to transmit power is defined in the Radar Range Equation in [8], p. 98f:

$$(15) \quad \frac{P_{Rx}}{P_{Tx}} = \sigma \frac{G_{Tx}(\theta_{Tx}) G_{Rx}(\theta_{Rx})}{4\pi} \left(\frac{\lambda}{4\pi R_1 R_2} \right)^2$$

Here, $G_{Tx}(\theta_{Tx})$ and $G_{Rx}(\theta_{Rx})$ describe the transmit gain and maximum receive gains in direction of the target, λ is the wavelength, and R_1 and R_2 are the distances to the scatterer from the transmit and receive antenna, respectively. The quantity σ represents the *radar cross section (RCS)* of the observed scene, a useful quantity when describing radar measurements. It is defined as “the area intercepting that amount of power which, when scattered isotropically, produces at the receiver a density which is equal to that scattered by the actual target” [3].

From that, the ratio of receive to transmit amplitude, which will be referred to as *channel gain*, can be defined as

$$(16) \quad C = \sqrt{\frac{P_{Rx}}{P_{Tx}}}$$

With that, the amplitude at the receiver can be expressed as

$$(17) \quad y_{Rx}(t) = C(\vec{r}_S) y_{Tx}(t - \tau)$$

$$(18) \quad = A_0 C(\vec{r}_S) e^{j(\omega_0(t-\tau) + \frac{1}{2} \dot{\omega}(t-\tau)^2 + \phi_0)}$$

The received signal is then mixed with a copy of the transmitted signal (12) and a band-pass filter is applied that removes undesirable frequencies. The resulting signal $y(t)$ is called *intermittent frequency* signal.

$$(19) \quad y(t) = \text{BP} \{ x_{RX}(t) \cdot x_{TX}(t) \}$$

$$(20) \quad = \text{BP} \left\{ A_0 e^{j(\omega_0 t + \frac{1}{2} \dot{\omega} t^2)} \cdot A_0 C(\vec{r}_S) e^{j(\omega_0(t-\tau) + \frac{1}{2} \dot{\omega}(t-\tau)^2)} \right\}$$

$$(21) \quad = A_0^2 C(\vec{r}_S) e^{j(\frac{1}{2} \dot{\omega} \tau^2 - \omega_0 \tau)} \cdot \text{BP} \left\{ e^{j(2\omega_0 t + \frac{1}{2} \dot{\omega} t^2 - \dot{\omega} \tau t)} \right\}$$

$$(22) \quad \approx C(\vec{r}_S) e^{-j\omega_0 \tau} e^{-j\dot{\omega} \tau t}$$

From this, the complex channel gain² $\underline{C}(\vec{r}_S)$ can be defined:

$$(23) \quad \underline{C}(\vec{r}_S) = C(\vec{r}_S) e^{-j\omega_0 \tau}$$

The fact that the IF-signal contains all the information – i.e. the IF signal’s frequency directly corresponds to the target’s distance – explains the main advantage of this technology. The carrier frequency can be orders of magnitude higher than the intermittent frequency, which drastically reduces the requirements for the subsequent signal processing, while retaining the improved resolution due to the smaller wavelengths of the carrier frequency [9].

²A way to interpret the complex channel gain is through S-parameters of a two-port network, since it relates the incident power wave at the transmit antenna’s port to the outgoing power wave at the receiver.

To locate a target in the cross-range dimensions, a single-channel FMCW-radar can be used to scan in multiple directions, by either rotating the antennas, redirecting their beam with rotating mirrors, or with beamforming antenna arrays. In any case, this requires highly directive antennas and also increases size, weight and cost of a radar sensor.

2.2. Multiplexing Techniques. Multiple-input multiple-output radar benefits from increased diversity and signal power. If N_{TX} transmit antennas and N_{RX} receive antennas are employed, $K = N_{TX} \cdot N_{RX}$ different signals can be extracted. To differentiate the signals from each other, a multiplexing technique has to be chosen. Options include time division multiplex, frequency division multiplex and code division multiplex.

In TDM, multiple access is achieved by the transmit antennas all send one after another, while all receive antennas receive simultaneously. In FDM, simultaneous transmission is made possible by subdividing the bandwidth and assigning a different frequency range to each antenna. That means that TDM allows for higher bandwidths for each transmission, while FDM allows higher transmission durations.

In CDM, both simultaneous transmission and use of the entire bandwidth is made possible by using a different waveform to each channel. However, processing at the carrier frequency is required to differentiate the signals from another, as opposed to TDM and FMD, where all processing can be done at the intermittent frequency range.

Depending on the application, a compromise has to be found between the advantages and drawbacks of each method. There are also methods available that combine aspects of these three basic paradigms, such as OFDM and Hadamard-Coding.[citation needed]

2.3. Multi-Channel FMCW. Once the received signals are demultiplexed, the ideal receive signal for antenna pair $k \in \{0, 1, \dots, K - 1\}$:

$$(24) \quad y_k(t) = \underline{C}_k e^{-j\dot{\omega}\tau_k t}$$

In reality, the scene can consist of an arbitrary number of scatterers (P), that each have their own radar cross section $\sigma_{p,k}, l \in \{0, 1, \dots, P - 1\}$ ³. Also, interference and electric noise may be present in each channel [see 9, ch. 4], which we summarize as $n_k(t)$. Thus, the overall IF-signal is:

$$(25) \quad y_k(t) = \sum_{s=0}^{L-1} \underline{C}_k(\vec{r}_s; \sigma_{l,k}) e^{-j\dot{\omega}\tau_k(\vec{r})t} + n_k(t)$$

After sampling the signal at sampling intervals T_s such that the sampling frequency $f_s = \frac{1}{T_s}$ is sufficiently high, i.e. fulfilling the Nyquist criterion: $2f_s > \frac{1}{2\pi}(\omega_0 + \dot{\omega}T_{chirp})$, and with M samples such that $MT_s < T_{chirp}$, the sampled IF-signal can be defined as:

$$(26) \quad y_k[m] = y_k(t = mT_s), \text{ for } m \in \{0, 1, \dots, M - 1\}$$

Since usually many successive chirps are transmitted and received, another index l can be added to identify the chirp (i.e. $y_k[m; l]$) In the data cube terminology that is primarily used for doppler radar, the sample index m regarding the time offset within a single chirp is referred to as the *short time* dimension, whereas the sample

³The index k is introduced here to take obstructed visibility into account: from the point of view of one channel, two scatterers may be visible simultaneously, while from the point of view of another, one might obstruct the other's visibility.

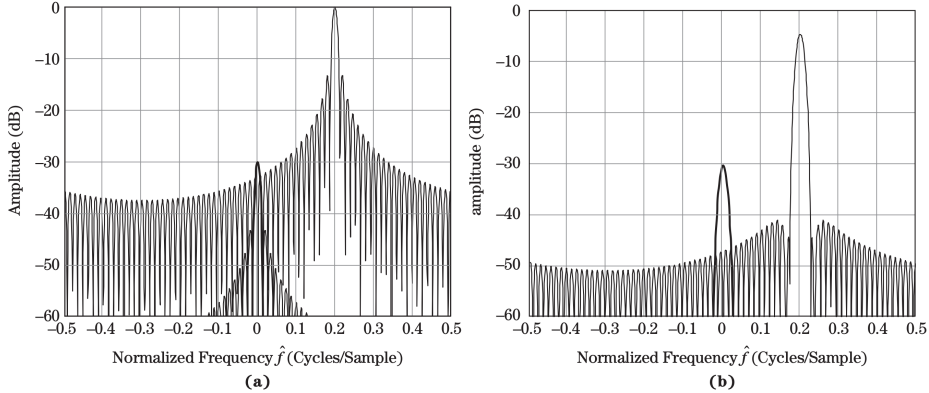


FIGURE 2.1. (a) Masking of a weak target response at $\hat{f} = 0$ by the sidelobes of a 30 dB stronger response at $\hat{f} = 0.2$. (b) Same two responses with Hamming window applied before the DTFT. Image and caption from [5, p.510]

index l regarding time offset between chirps is known as the *long time* dimension [see 5, pp. 290f.].

2.4. Discrete Fourier Transform. An important tool in digital signal processing is the *discrete Fourier transform (DFT)*. It is widely used to compute the frequency spectrum of a given discrete time signal. The DFT spectrum $Y[n]$ of a discrete signal $y[m]$ is computed as follows:

$$(27) \quad Y[n] = \sum_{m=0}^{M-1} y[m] e^{-j \frac{2\pi n}{N} m}$$

An alternative formulation computes a continuous spectrum $Y(\Omega)$ from the discrete input signal:

$$(28) \quad Y(\Omega) = \sum_{m=0}^{M-1} y[m] e^{-j \Omega m}, \Omega \in [-\pi, \pi]$$

A highly efficient implementation of the DFT is the FFT algorithm, which, for a given data size n , reduces the runtime of the regular DFT $\mathcal{O}(n^2)$ to $\mathcal{O}(n \log n)$ [1].

In [5, pp. 509–513] explains the necessity of windowing when using the FFT. To summarize, the FFT works under the assumption that its input time signal continues periodically before and after the supplied set of samples. Thus, any discontinuities between the first and last sample show in the spectrum as spectral leakage. This spectral leakage can mask weaker spectral components, as illustrated in Figure 2.1a.

To address this issue, so-called *window functions*, also known as *tapering functions*, can be applied to the input signal. These functions gradually reduce the amplitude of the signal at the edges, effectively fading it in and out. By doing so, they remove the discontinuities that cause spectral leakage, thus mitigating problems like masking, as illustrated in Figure 2.1b.

2.5. Virtual Antenna Arrays. An important concept in analyzing MIMO arrays is that of the *virtual antenna array*: in a nutshell, the idea is to express the $N_{TX} \times N_{RX}$ MIMO array as an equivalent $1 \times K$ SIMO array. The procedure to construct the corresponding virtual array for a given MIMO array is as follows:

The transmit antenna associated with channel $k = 0$ is placed in the origin of the virtual array's coordinate system. Then, K receive antennas are placed such that the displacement between them and the transmit antenna is the same as it was between the original MIMO array's corresponds transmit and receive antenna. It is possible for virtual antennas to overlap. As we will see later, the input signal under far-field conditions only depends on the relative displacement between the Tx- and Rx-antennas of a channel, and not their absolute positions.

An example MIMO array and its corresponding virtual array can be seen in figures a and b, respectively. The numbering convention for channel index k corresponding to transmit antenna i and receive antenna j , that is also used throughout the thesis is as follows:

$$(29) \quad k = N_{Tx}i + j$$

In our example, the virtual transmit antenna with $k = 5$ corresponds to $(i, j) = (1, 2)$.

3. Image Reconstruction

Image reconstruction is an inverse problem where the position \vec{r} and RCS of the scatterers σ has to be estimated from the received signals $y_k[m]$. A wide range of approaches is available. A common on spectral analysis of the signals enabled by the *discrete Fourier transform (DFT)*. More flexibility is provided by backprojection (also known as the inverse Radon transform). More sophisticated algorithms include MUSIC, ESPRIT and PARAFAC.

In the following, three approaches and their application to the problem of image reconstruction for FMCW MIMO radar sensors are discussed. In this thesis, the DFT- and backprojection based approaches are implemented and evaluated for a MIMO radar system. The MUSIC algorithm is also briefly introduced to give an indication of its complexity.

3.1. FFT-based Imaging. In this approach, the FFT is applied over three dimensions of the input signal, obtaining a discrete output signal in spherical coordinates whose amplitude is an estimate of the locational reflectivity.

For each input channel, the range of a target can be estimated by applying the DFT over time. The resulting spectrum's peak corresponds to the target:

$$(30) \quad \mathcal{F}_m\{y_k[m]\}(\Omega) = \sum_{m=0}^{M-1} e^{-j2\pi \frac{m\Omega}{M}} y_k[m]$$

$$(31) \quad = \underline{C}_k(\vec{r}_S) \delta(\Omega - \dot{\omega}\tau_k(\vec{r}_S)T_s)$$

In order to understand how information on the direction of a target can be extracted from the channel data, we consider an ideal $1 \times K$ horizontal ULA where the spacing is exactly $d = \frac{\lambda_0}{2}$, with $\lambda_0 = \frac{c_0}{f_0}$. The antennas are located at $\vec{r}_{TX} = \vec{0}$ and $\vec{r}_{RX,k} = (kd, 0, 0)^T$. A scatterer located at $\vec{r}_S = (r_S \sin \theta_S, r_S \cos \theta_S, 0)^T$ reflects the transmitted radar waves with an intensity of A_S . Then, their runtime across the array is:

$$(32) \quad \tau_k = \frac{1}{c_0} (\|\vec{r}_{TX} - \vec{r}_S\| + \|\vec{r}_{RX} - \vec{r}_S\|)$$

In far-field conditions, the target is far enough ($r \gg Kd$) away for the reflected wavefronts to be planar. That means that a first-order approximation for the

runtime can be used:

$$(33) \quad \tau_k \approx \frac{2r_S + kd \sin \theta_S}{c_0}$$

In equation (23), it can be seen that the channel gain $C_k(\vec{r})$ contains a phase shift depending on the runtime of the waves:

$$(34) \quad \underline{C}_k(\vec{r}) = C_k(\vec{r}_S) e^{-j\omega_0 \tau_k}$$

$$(35) \quad = C_k(\vec{r}) e^{-j\frac{\omega_0}{c_0}(2r_S + kd \sin \theta_S)}$$

For a uniform array under far-field conditions, the complex channel gains can be assumed only differ in phase. That means that

$$(36) \quad \underline{C}_k(\vec{r}) = C_k(\vec{r}) e^{-j\frac{\omega_0}{c_0}(2r_S + kd \sin \theta_S)}$$

$$(37) \quad = C_k(\vec{r}) e^{-j\frac{\omega_0}{c_0}2r_S} e^{-j\frac{\omega_0}{c_0}kd \sin \theta_S}$$

$$(38) \quad = \underline{C}_0(\vec{r}) e^{-j\frac{\omega_0}{c_0}kd \sin \theta_S}$$

Therefore, if the FFT is applied accross the ULA, the resulting spectrum is:

$$(39) \quad \mathcal{F}_k\{y_k[m]\}(\Omega) = \mathcal{F}_k\{y_0[m]e^{-j\frac{\omega_0}{c_0}kd \sin \theta_S}\}(\Omega)$$

$$(40) \quad = y_0[m] \cdot \delta\left(\Omega - \frac{\omega_0}{c_0}(d \sin \theta_S)\right)$$

$$(41) \quad = y_0[m] \cdot \delta(\Omega - \pi \sin \theta_S)$$

$$(42)$$

The azimuth angle θ_S can be extracted from the signal supplied by a horizontal ULA. Analogously, the elevation angle ϕ_S can be obtained with a vertical ULA. If a $1 \times K$ virtual array is used, where the K receive antennas form a *uniform rectangular array (URA)*, successive DFTs across the rows and columns of this grid yield two dimensions.

Overall, a 3D image in range, azimuth, and elevation is generated by calculating the DFT over time, and the DFTs over the rows and columns of the virtual array. For this to work, the scatterer needs to be distant enough for the wavefronts to be planar, and the virtual array's grid needs to be uniformly spaced with $d = \lambda_0/2$ spacing.

3.2. Backprojection Imaging. Compared to the FFT-based approach, back-projection takes fewer approximations and requirements on the array to work, while theoretically using a similar amount of computation. The approach works by correlating the input signal $y_k[m]$ to the theoretical signal $s_k[m, \vec{r}]$ of an ideal scatterer at different locations. The mean correlation of all channels to the theoretical signal is then used as an estimate for the recorded scene $\hat{F}(\vec{r})$:

$$(43) \quad \hat{F}(\vec{r}) = \frac{1}{K} \sum_{k=0}^{K-1} s_k[m, \vec{r}] \star y_k[m]$$

$$(44) \quad = \frac{1}{K} \sum_{k=0}^{K-1} \sum_{m=0}^M s_k^*[m, \vec{r}] y_k[m]$$

Using the signal model from (24) yields:

$$(45) \quad \hat{F}(\vec{r}) = \frac{1}{K} \sum_{k=0}^{K-1} \sum_{m=0}^M \underline{C}_k^*(\vec{r}) e^{+j\omega_0 \tau_k(\vec{r}_S)m T_s} y_k[m]$$

To reduce the computational intensity of this algorithm, a hybrid approach[6] proposes that calculating the inner sum (over m) can be rewritten as an inverse discrete fourier transform (IDFT):

$$(46) \quad \hat{F}(\vec{r}) = \frac{1}{K} \sum_{k=0}^{K-1} \underline{C}_k^*(\vec{r}) \sum_{m=0}^M e^{+j\dot{\omega}\tau_k(\vec{r}_S)mT_s} y_k[m]$$

$$(47) \quad = \frac{1}{K} \sum_{k=0}^{K-1} \underline{C}_k^*(\vec{r}) \sum_{m=0}^M e^{j\Omega m} y_k[m] \Big|_{\Omega=\dot{\omega}\tau_k(\vec{r}_S)T_s}$$

$$(48) \quad = \frac{1}{K} \sum_{k=0}^{K-1} \underline{C}_k^*(\vec{r}) \mathcal{F}_m^{-1} \{y_k[m]\} (\Omega = \dot{\omega}\tau_k(\vec{r}_S)T_s)$$

In practice, the result of the inverse FFT is not continuous in Ω as suggested above, but rather only available at a set number of sample points n . The resulting error can be reduced by zero-padding the input to the inverse FFT, increasing the amount of sampled frequencies.

3.3. MUSIC Imaging. The Multiple Signal Classification (MUSIC) algorithm [2] is also widely used in radar imaging (). In our case, it operates on the time-domain fourier transform of the IF-signal, and makes similar far-field approximations as the DFT-based approach. The abstract signal model for MUSIC is:

$$(49) \quad \mathbf{y}(t) = \mathbf{A} \cdot \mathbf{s}(t) + \mathbf{n}(t)$$

Here, $\mathbf{y}, \mathbf{n} \in \mathbb{C}^K$, $\mathbf{A} \in \mathbb{C}^{K \times Z}$, and $\mathbf{s} \in \mathbb{C}^Z$. Z is the number of voxels in the output image and K the number of receive channels. For example, if the output image consist of $X \times Y \times Z$ cuboid voxels, then $Z = X \cdot Y \cdot Z$.

Thus, the support matrix \mathbf{A} is a linear transform from the locational reflectivity \mathbf{s} to the expected input signal vector \mathbf{y} . Each column vector \mathbf{a}_z of the support matrix \mathbf{A} therefor corresponds to the expected input signal vector caused by a point source.

The MUSIC algorithm revolves around the correlation matrix of its input signal \mathbf{R}_{yy} . Assuming the a stationary scene with zero-mean noise of covariance \mathbf{C}_{nn} , it follows that

$$(50) \quad \mathbf{R}_{yy} = E\{\mathbf{y}\mathbf{y}^H\}$$

$$(51) \quad = \mathbf{A}\mathbf{R}_{ss}\mathbf{A}^H + \mathbf{C}_{nn}, \text{ with } \mathbf{R}_{ss} := E\{\mathbf{s}\mathbf{s}^H\}$$

Assume that \mathbf{R}_{ss} is nonsingular with rank q and that \mathbf{A} has full rank. If \mathbf{R}_{yy} has p eigenvalues, then the smallest $p - q$ of them are all σ^2 , and their corresponding eigenvectors – i.e. the columns of \mathbf{C}_{nn} – are all orthogonal to the support vectors \mathbf{a}_z .

This property is key to the MUSIC algorithm. The metric used to generate an image is the projection of \mathbf{a}_z onto the \mathbf{C}_{nn} . Due to their orthogonality, the projection of support vectors corresponding to a signal source will be zero. The image intensity at voxel z is thus defined computed as the normalized inverse square magnitude of this projection:

$$(52) \quad P_{MUSIC}[z] = \frac{\mathbf{a}_z^H \mathbf{a}_z}{\mathbf{a}_z^H \hat{\mathbf{C}}_{nn}^H \hat{\mathbf{C}}_{nn} \mathbf{a}_z}$$

The input signals are often highly correlated, due to phenomena such as multi-path propagation or inter-channel crosstalk. This unfortunately means that nonsingularity of \mathbf{R}_{ss} and thereby of \mathbf{R}_{yy} cannot always be guaranteed. A preprocessing step is required to “decorrelate” the signals and thereby making \mathbf{R}_{ss} singular again.

While early schemes, such as the “3/4in plywood” spacial dither algorithm by Widrow *et al.* [CITE] consisted of mechanically moving the receive antenna array orthogonal to the look direction, preprocessing can also be done after receiving the signal. Spacial smoothing, as employed in [CITE], is one such method.

Although MUSIC can achieve high fidelity imaging, it is also rather computationally intensive. For high numbers of channels and/or high image resolutions, the computational intensity may become prohibitive for application.

3.4. Complexity Analysis. Suppose M samples are available for the K channels of an $N \times N$ uniform rectangular array. The fastest of the three algorithms is the FFT-based algorithm. It first applies an FFT to each of the $K = N^2$ channels. Then, the azimuth FFT is applied to the each of the N horizontal sub-arrays for each of the M range bins. Finally, the elevation FFT is applied to the each of the N vertical sub-arrays for each of the M range bins. The resulting image has a resolution of $M \times N \times N$. The total runtime comes out to:

(53)

$$N^2\mathcal{O}(M \log M) + 2MN\mathcal{O}(N \log N) = \mathcal{O}(MN^2 \log(MN^2)) = \mathcal{O}(MK \log MK)$$

Backprojection’s runtime scales linearly with the target resolution of the image. If the target image consists of Z different voxels, then for each voxel, K channels worth of M weights each are calculated, and each applied to the M samples of that channel. The results are then summed up resulting in the amplitude of each voxel. The overall runtime is:

(54)

$$Z((\mathcal{O}(MK) + \mathcal{O}(M^2K) + \mathcal{O}((M-1)(K-1)))) = \mathcal{O}(ZM^2K)$$

It can be improved by the aforementioned hybrid approach: For each of the K channels, one M -point FFT is calculated, and Z weights are applied to the FFT evaluated at the corresponding frequency. That brings the total runtime down to:

(55)

$$K(\mathcal{O}(M \log M) + \mathcal{O}(Z)) = \mathcal{O}(K(Z + M \log M))$$

The runtime of MUSIC is substantially higher. For each of the K channels, one M -point FFT is calculated. After that, for each of the M ranges, a $K \times K$ covariance matrix is computed. The singular value decomposition [cite pdf for runtime] of each of these matrices is computed and the noise subspace is extracted. The C columns of the support matrix are then projected onto the noise subspace to compute the intensity at that voxel. The resulting image has a resolution of $M \times C$, and the total runtime is:

(56)

$$K\mathcal{O}(M \log M) + M(\mathcal{O}(K^2) + \mathcal{O}(K^3) + C\mathcal{O}(K^2))$$

(57)

$$= \mathcal{O}(K^3M + KMC + KM \log M)$$

CHAPTER 3

Hardware Evaluation

This chapter starts with a brief introduction of the sensor employed in this thesis(sec. 1). The system properties and specifications are outlined, and the makeup of the antenna array is described. On the basis of this knowledge, the system can be evaluated through a number of experiments.

The second part of this chapter (sec. 2) focuses on stability analysis, which is conducted through long-term static measurements of a corner reflector. By monitoring the radar system's performance over an extended period, we aim to assess its stability and reliability in real-world operating conditions. The analysis provides insights into any temporal variations or drifts in system parameters, enabling proactive measures to mitigate potential sources of error.

The third part of this chapter (sec. 3) focuses on antenna gain measurements using a rotating setup. Antenna gain plays a crucial role in radar imaging, affecting the system's sensitivity and resolution. By rotating the radar system and precisely measuring the received signals from known targets, we can accurately determine the antenna gain across different azimuth angles. This measurement process enables the characterization and validation of antenna performance, facilitating improved imaging accuracy and consistency.

Through these procedures, Chapter 3 aims to establish a robust foundation for the subsequent imaging algorithms that are implemented and evaluated in Chapter 4. By ensuring the stability of system parameters and accurately characterizing antenna performance, we strive to enhance the reliability and effectiveness of FMCW MIMO radar imaging for various applications.

1. Indurad Multi-Channel Radar

The sensor employed in this thesis operates on Multiple Input Multiple Output (MIMO) Frequency Modulated Continuous Wave (FMCW) technology, showcasing advanced features tailored for precise radar imaging.

- applications

1.1. System Parameters. Table 1 summarizes the key technical characteristics of the sensor. The iMCR offers a range capability of up to 100 meters, extendable to 800 meters with active beamforming techniques. The sensor achieves a remarkable range resolution of 3.8 mm, enabling detailed imaging of objects within its detection range. Utilizing a sawtooth or chirp signal type, the sensor employs Time Division Multiplexing (TDM) in transmission for efficient multiplexing. Operating within the frequency range of 77 GHz to 81 GHz, it leverages the millimeter-wave spectrum to achieve high-resolution imaging suitable for a variety of applications. The chirp duration of the sensor is between about 60 GHz to 70 GHz, ensuring effective signal processing and data acquisition. Equipped with 12 transmit antennas and 16 receive antennas, the sensor offers comprehensive coverage and sensitivity, facilitating robust imaging performance. Furthermore, the sensor's Intermediate

Radar Characteristic	iMCR
Technology	mmWave FMCW MIMO
Maximum Range	100 m (800 m with active beamforming)
Range Resolution	3.8 mm
FM Type	Sawtooth/Chirp
Multiplexing	TDM in Tx
Frequency	77 GHz to 81 GHz
Chirp Duration	60 μ s to 70 μ s
Antennas	12 Tx, 16 Rx
IF Samplerate	22 MHz

TABLE 1. iMCR: Technical Overview



FIGURE 3.1. The iMCR Sensor. closed housing (left) and open housing (right)

Frequency (IF) samplerate is set at 22 MHz, providing sufficient bandwidth for accurate signal processing and analysis. This combination of advanced features and specifications positions the sensor as a versatile and effective tool for radar imaging tasks in diverse scenarios, ranging from automotive safety systems to industrial sensing applications.

Figure 3.1 shows the sensor in a watertight closed housing, and an open housing. The closed housing is ideal for mining applications, but for development purposes, the open housing may be preferable since it has no impact on the input signals.

The system can be subdivided into a frontend and a backend. The frontend consists of the antennas, and the transmitter and receivers. The transmitters and receivers are implemented through a cascaded setup of four Texas Instruments® AWR2243P™ chips.

The backend enables integration of the sensor into imaging applications. It consists of an FPGA that is used for receiving data from the frontend and its configuration, and a computer running an embedded Linux system. The software

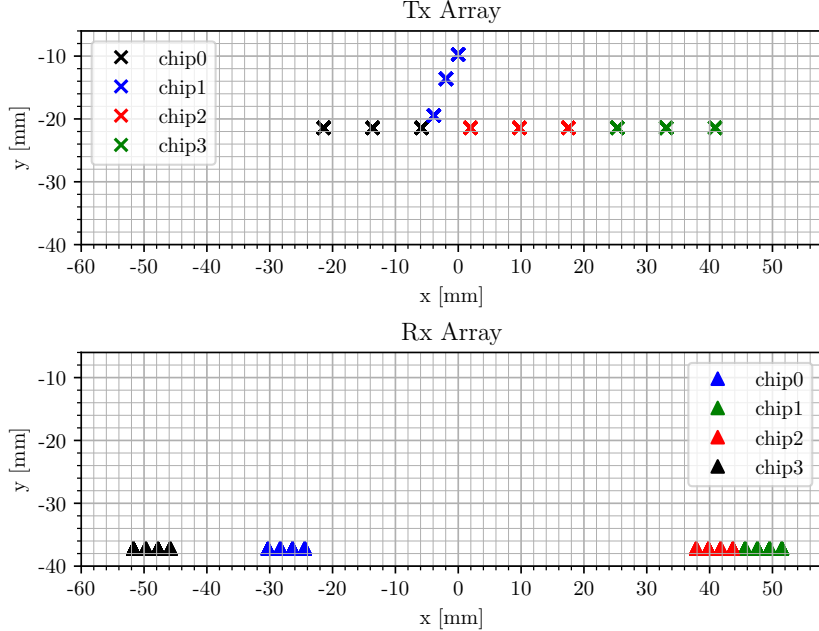


FIGURE 3.2. iMCR transmit and receive antenna positions

running on this system operates the FPGA and sends the received radar data through TCP.

1.2. Virtual Antenna Array. As described in subsection 2.5, a virtual antenna array is the far-field equivalent SIMO array that can be derived for a given MIMO array. It is also a useful tool to gain an intuition on the resolution capabilities of an array.

Figure 3.2 shows the physical positions of the transmit and receive array. The transmit array consist of four groups of three antennas. Apart from one group, they are evenly spaced horizontal at the same height, with a distance of $4d = 2\lambda_0$ between the members of a group. The exception is made by the antennas driven by chip 1, which are located at different heights. The receive array consists of four groups physically separated of four antennas that are spaced exactly $d = \lambda_0/2$ apart horizontally. They are all at the same height.

Figure 3.3 shows the corresponding virtual array. Due to the distribution of antennas in the physical array, all antennas in the virtual array fall exactly onto a grid with $\lambda_0/2$. The majority of the virtual antennas is located at the same height. Indeed, some elements in the virtual array even overlap. In the following, these elements will be referred to as the *azimuth array*. The remaining elements are at different heights, and will be referred to as the *elevation channels*.

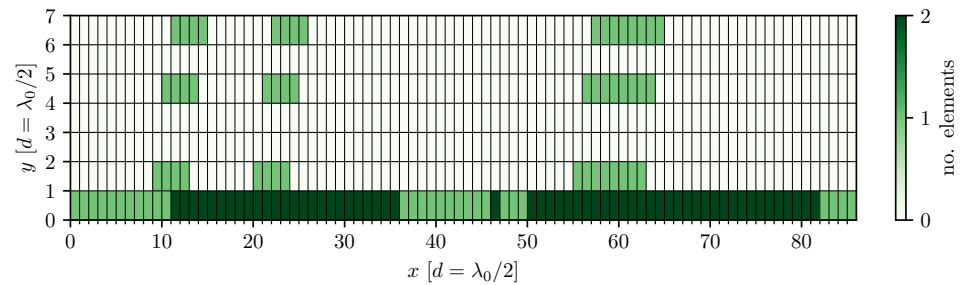


FIGURE 3.3. iMCR virtual array

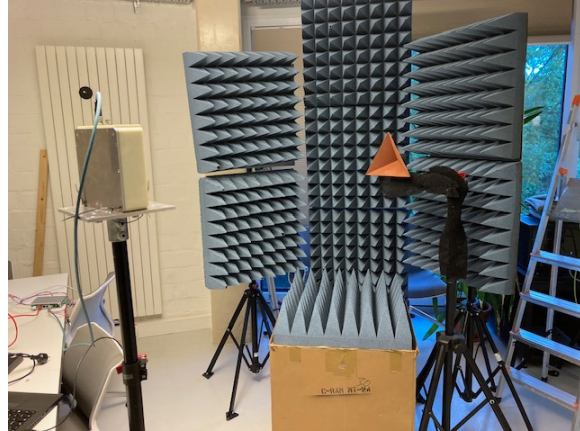


FIGURE 3.4. Measurement Setup

2. Stability Analysis

The imaging algorithms introduced in the previous chapter all rely on a radar system with constant characteristics. We begin by discussing the physical setup of the experiment, outlining the equipment used and the experimental conditions.

Additionally, we discuss the preprocessing steps and define the quantities analyzed to assess system stability accurately. These steps are essential for mitigating noise and ensuring the integrity of the data used for stability analysis.

Furthermore, we explore the concept of self-calibration upon system restart, investigating how the radar system automatically recalibrates to maintain accuracy and consistency. Understanding this process is crucial for interpreting stability analysis results accurately and implementing corrective measures effectively.

Finally, we examine the differences between antennas and their impact on radar stability. Variations in antenna characteristics, such as gain, directivity, and polarization, can affect signal reception and transmission, influencing the system's overall stability, and thereby impacting the imaging fidelity.

2.1. Setup. The experiment conducted to explore the stability of the sensor consists of setting it up in a low-reflection environment and placing a corner reflector at boresight in front of the sensor at a distance of roughly 1 m (cf. 3.4).

A measurement at relatively short range is preferable because the signal level is higher, reducing the impact of noise. The time data collected in all channels is recorded every minute, and the temperature readings of the sensor's CPU, FPGA and radar frontend are also recorded every minute (cf. 3.5a).

Due to the static geometry of the setup, the runtime of each transmitted waveform should be identical. Thus, the ideal deramped signal should be of a single, constant frequency and without inter-channel phase differences. For analysis, system runtime and temperature cannot be considered independent variables, as illustrated in Figure 3.5b: The system starts at ambient temperature, heating up and approaching a stable operating temperature on turning on (t_0), and cooling back down after turning off (t_1).

In practice, the spectral peak caused by the reflector will also have a certain bandwidth, and other peaks at higher and lower frequencies will be present due to incomplete shielding and/or unwanted reflections. Also, the reflector peak may wander if the setup geometry moves.

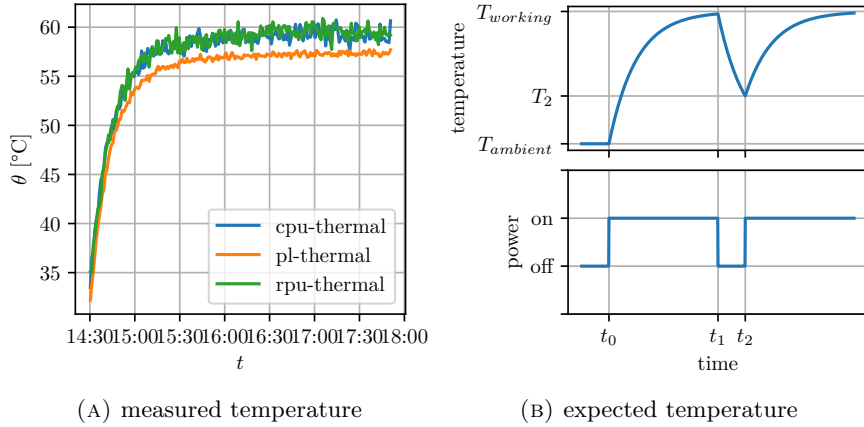


FIGURE 3.5. Time Evolution of the Radar System's Temperature

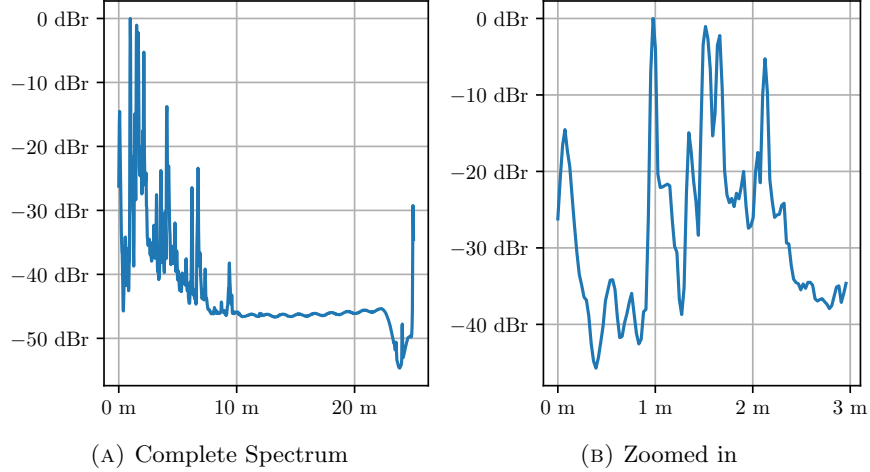


FIGURE 3.6. Mean Intensity Spectrum

2.2. Preprocessing and Analysis. The primary objective of this experiment is to determine whether the system characteristics remain constant over time. This objective can be distilled into an examination of the channel gains \underline{C}_k . Because of the aforementioned imperfections in the experiment, some preprocessing is required to analyze the systematic offsets present in the radar signal. Multiple additional peaks in the spectrum are visible in Figure 3.6. It is therefore prudent to limit the analysis to only the FFT-bin at the maximum of the peak caused by the reflector. In theory, this FFT-bin should contain the exact channel gain (see also Equation 31):

$$(58) \quad \hat{\underline{C}}_k[l] = \mathcal{F}\{y_k[m; l]\}|_{\Omega=\hat{\Omega}[l]}$$

$$(59) \quad \text{with } \hat{\Omega}[l] = \arg \max_{\Omega} |\mathcal{F}\{y_k[m; l]\}(\Omega)|$$

In practice, the measurement environment exhibits some minor changes, for example in temperature and humidity, which can result in the geometry to shift by up to a few millimeters. This shows by the spectral maximum shifting over time, as seen in Figure 3.7.

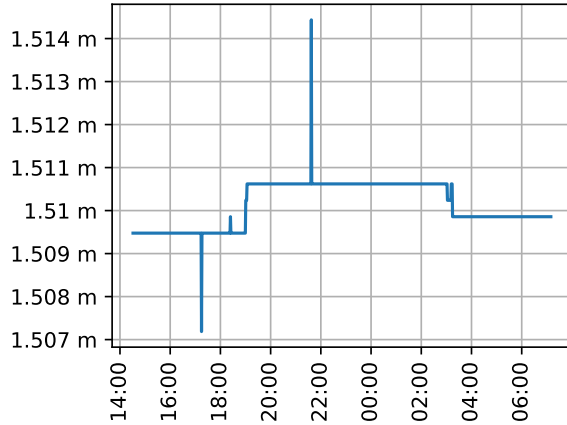


FIGURE 3.7. Change in reflector distance as measured by iMCR

The main metric used to assess the stability of the channel gains in the following analysis will be the *channel gain drift* \underline{D}_k , defined as the complex ratio of the maximum FFT-bin in range to its initial value:

$$(60) \quad \underline{D}_k[l] = \frac{\hat{C}_k[l]}{\hat{C}_k[0]} = \frac{\mathcal{F}\{y_k[m; l]\}(\hat{\Omega})}{\mathcal{F}\{y_k[m; 0]\}(\hat{\Omega})}$$

Using a logarithmic representation of this ratio, it can be represented in terms of a level difference in dBr and a phase difference in degrees.

2.3. Effects of System Temperature and Runtime. Multiple measurements have indicated that, while the amplitude rarely varies by more than 1 dB, the phase is not as stable over time. Typically, the mean phase drifts by up to 50° in the hours after system startup, with the rate of change reducing after around four hours. However, it has to be noted that there is no clear correlation between phase drift and temperature: the phase continues to drift after the system temperature stabilizes; the reduction in drift only occurs hours after the system has reached a stable temperature of approximately 60°C .

2.4. Differences between Antennas. To further investigate the time evolution of the channel gain drifts, their impact can be described in terms of relative antenna gains. As stated in Equation 15f., each the squared gain of a channel k is proportional to the gains of the two antennas i and j that make up the channel. That is,

$$\underline{D}_k^2 = \frac{\hat{C}_k^2[l]}{\hat{C}_k^2[0]} = \frac{G_{Tx,i}[l]}{G_{Tx,i}[0]} \frac{G_{Rx,j}[l]}{G_{Rx,j}[0]}$$

Defining Rx antenna 0 as a reference, i.e. $G_{Rx,0}[l] = 1$ leads to a simple way of extracting the Tx antenna gain drift:

$$\frac{G_{Tx,i}[l]}{G_{Tx,i}[0]} = \underline{D}_k^2[l] \Big|_{k=N_{Tx}i}$$

With knowledge of that parameter, the Rx antenna drifts can be estimated using the remaining drift measurements:

$$\frac{G_{Rx,j}[l]}{G_{Rx,j}[0]} \approx \frac{1}{N_{Tx}} \sum_{i=0}^{N_{Tx}-1} D_k^2[l] \Big|_{k=N_{Tx}i} \cdot \left(\frac{G_{Tx,i}[l]}{G_{Tx,i}[0]} \right)^{-1}$$

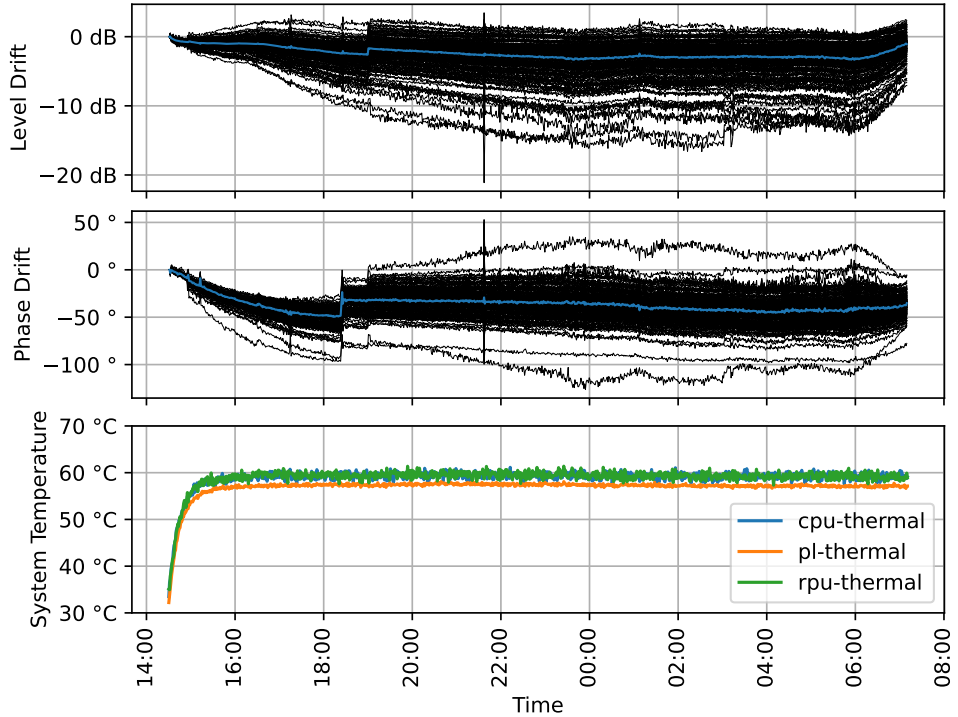


FIGURE 3.8. Recorded drift over night

The results of this are shown in 3.9.

It can be seen that all antenna gains drift from their initial value by a similar amount. They tend to be similar in amplitude and phase to other antennas on the same chip. The effects of interference events, such as the 1 mm shift at around 18:30 (c.f. 3.7), may differ between the antennas.

2.5. Effects of Self-Calibration. As described in section 1, the AWR2243P-chips undergo a self-calibration upon initialization. This initialization can be triggered by either restarting the entire system or by re-writing the configuration registers on the radar chips. Indeed, this initial calibration can be observed in the data (cf. 3.10). After the initial system restart, there is an escalation in incoherence, manifesting in a broader distribution of drift in both level and phase. The level in each channel experiences a slight increase, with an approximate rise of 0.3 dB. Additionally, the mean phase drift undergoes alterations of up to 5°.

TODO: graph jumps to new phase before reboot. confirm or fix.

TODO: quantify amount of discontinuity

2.6. Conclusion. The systematic offsets of the system are now better described. While the amplitude of the measured signal is relatively stable, the phase is affected more strongly. All channels' phases drift from both their initial value and each other over time. It has also been shown that restarting the radar frontend has an effect on the phase, since the frontend undergoes an automatic calibration each time. No clear bias within the array has been found, seeing that across multiple measurements, all channels seem to be affected similarly.

Overall, it has been demonstrated that the radar system cannot be considered ideal and its imaging fidelity will be affected by the growing incoherence during

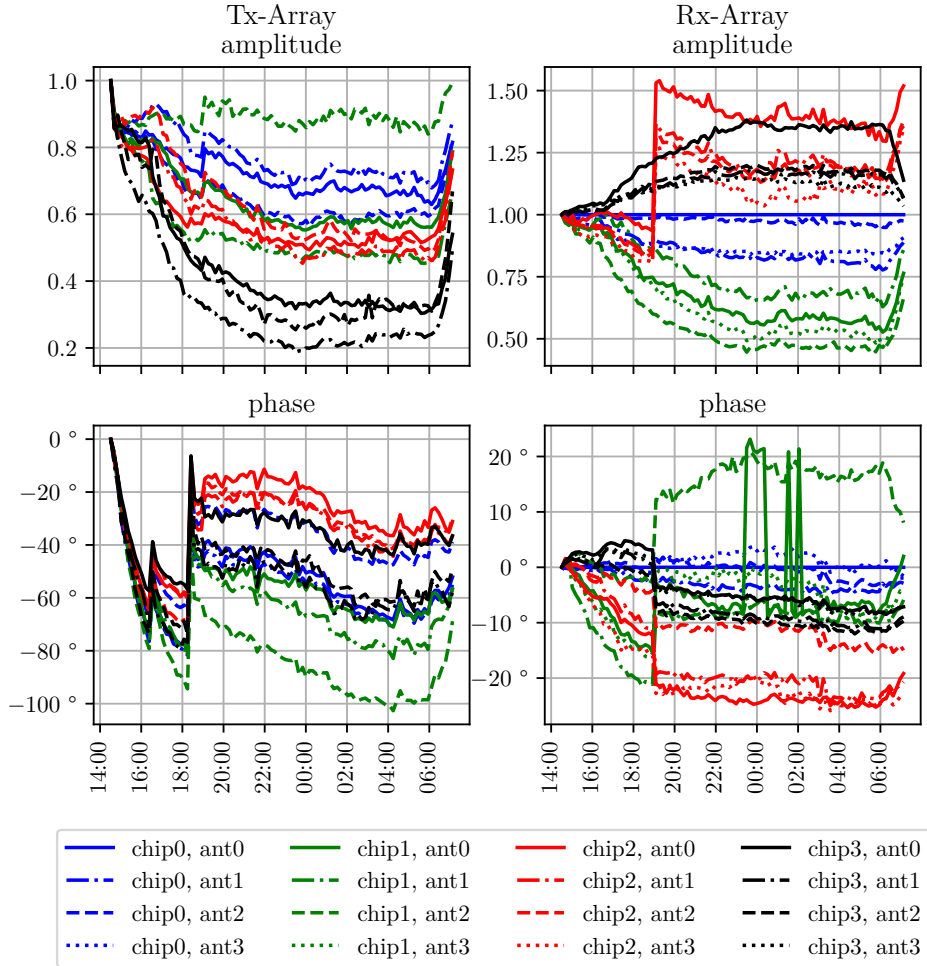


FIGURE 3.9. Drift by Antenna

long runtimes. Furthermore, restarting the system will change the systematic offsets due to the automatic calibration of the radar frontend hardware. Adaptive online calibration would be required to deal with these effects.

To limit the scope of this thesis, the focus is set on the offline-part of the calibration process. Because the phase and amplitude offsets are affected by the automatic calibration of the system, this calibration should ideally be repeated on every startup, ideally letting the system temperature stabilize.

An advantage for the offline calibration is that the speed at which the array incoherence grows is limited. That means that for sufficiently short runtimes, it can be assumed to be static, and therefore, an offline calibration to be sufficient.

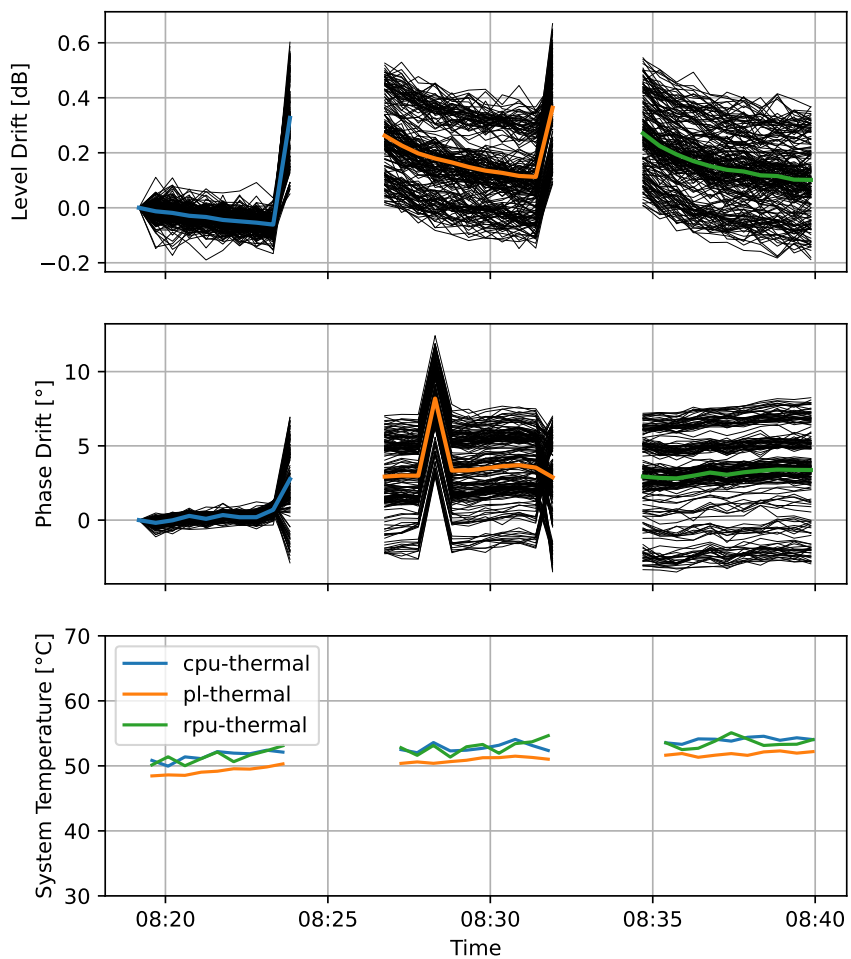


FIGURE 3.10. Recorded drift and temperature with system restart

3. Antenna Characteristics

In this section, the array's antenna gains are measured and then analyzed. The measured antenna gains can then directly be employed as weights for the backprojection algorithm, resulting in a calibrated array. A subset of the extracted parameters can also be employed for offline calibration when using FFT-based imaging.

3.1. Experiment Setup. TODO: include photo The experiment conducted to measure the array's antenna gain patterns was conducted outdoors. This is preferable because the experiment requires more physical space than the previous stability analysis, and of course minimal interfering clutter in that space. The sensor is mounted on a vertical rotating axis, and a corner reflector is placed in front of the sensor. Rotating the axis allows the sensor to observe the corner reflector from multiple angles, while retaining a fixed distance. Doing this can be used to measure the antenna gains in azimuth; to measure the antenna gains in elevation, the sensor is mounted on the same axis to rotate around its horizontal axis. These two measurements are repeated for multiple reflector distances.

While the relative position of the rotating axis can be recorded with a decent resolution of around 0.01° , the absolute positioning of the reflector is hard to achieve with the same accuracy. The sensor itself can however be used to improve positioning accuracy: during setup, the phase of the peak caused by the reflector is extracted with a similar method as in section 2 and displayed. Minimizing the phase differences between the array's channels by fine-tuning the reflector's position ensures that it be located at boresight. These measurements are repeated with multiple distances of the reflector.

The field on which the experiment was set up is widely void of clutter, but not entirely. Several trees and brushes are located at the edge of the scene. Extra interference and reflections are caused by the floor. It is also not perfectly level, varying in height by up to 1 m, which means that the reflector is not always exactly at the same height. The sensor mount also causes some problems [NEEDS DRAWING]: when the sensor is mounted on its inside, the rotational axis passes exactly through the antenna array's plane, but some shading occurs when the reflector is on the same side as the sensor mount's diagonal reinforcement. When the sensor is mounted on the outside, the rotational axis is no longer in the antenna array's plane, adding complexity and inaccuracy to the subsequent analysis.

3.2. Preprocessing and Analysis. The objective of the subsequent analysis is to extract the antenna gains from the measured IF-signals. In subsection 2.1, the ideal deramped signal $y_{kl}[m]$ from channel k at long-time index l for a single reflector at position \vec{r}_l is defined in equation (15) :

$$y_{kl}[m] = C_k(\vec{r}_l) e^{-j\omega_0 \tau_{kl}} e^{-j\dot{\omega} \tau_{kl} m T_s}$$

The square channel gain directly relates to the antenna gains A_i and B_j of the transmit antenna with index i and the receive antenna with index j that make up the channel:

$$C_k^2 = \frac{P_{Rx}}{P_{Tx}} = G_{Tx}(\theta, \phi) G_{Rx}(\theta, \phi) \frac{\sigma}{4\pi} \left(\frac{\lambda}{4\pi R_1 R_2} \right)^2$$

For simplicity's sake, the following quantities are defined:

$$(61) \quad c_k(\theta, \phi) := \frac{C_k(r, \phi, \theta)}{\max |C_k(r, \phi, \theta)|}$$

will be called the *channel characteristic*, and assumed to be constant in r with $c_k(\theta, \phi) \in [0, 1]$. The *antenna gains* are the relative maximum antenna gains of the transmit and receive antennas:

$$(62) \quad \underline{A}_i := \frac{\max G_{Tx,i}(\theta, \phi)}{G_{Rx,0}(\theta, \phi)} e^{j\psi_i}$$

$$(63) \quad \underline{B}_j := \frac{\max G_{Rx,j}(\theta, \phi)}{G_{Rx,0}(\theta, \phi)} e^{j\vartheta_j}$$

As defined in Equation 29, each channel k has a corresponding transmit antenna i and a receive antenna j . All antenna gains are defined with regards to the reference antenna, receive antenna 0. They also include a phase offset which describe any mismatches in the individual antenna, such as polarization, reflections in the antenna ports or length offsets in the transmission lines leading to them.

With that, the radar range equation can be rewritten as follows:

$$\underline{C}_k^2 = \underline{A}_i \underline{B}_j c_k^2(\theta, \phi) e^{j2(\varphi_k - \omega_0 \frac{R_1 + R_2}{c_0})} \frac{\sigma}{4\pi} \left(\frac{\lambda}{4\pi R_1 R_2} \right)^2$$

The goal of the subsequent analysis is twofold: to extract all parameters of the above signal model while identifying and removing interference through processing.

Limiting the analysis to a single range bin will work towards both reducing interference and extracting parameters: ideally, the DFT spectrum of the IF signal consists of just a single peak, weighted with the channel gain $C_k(\vec{r})$ (see Equation 31). Thus, the channel gain can be extracted if the correct bin $\hat{\Omega}$ is picked:

$$(64) \quad \hat{\Omega} = \dot{\omega} \tau_k(\vec{r}_S) T_s$$

$$(65) \quad = \dot{\omega} \frac{R_1 + R_2}{c} T_s$$

$$(66) \quad \Rightarrow \mathcal{F}_m\{y_k[m]\}(\Omega = \hat{\Omega}) = \underline{C}_k(\vec{r}_S)$$

3.3. Range Estimation. In order to improve the accuracy of the subsequent analysis, the exact position of the reflector is estimated from the radar data. To do this, numerical optimization is employed to find the parameter set $\hat{R}_s, \hat{\theta}_s, \hat{\epsilon}$ that minimizes the difference between a range estimate $\hat{R}_{k,l}$ and the range spectral peak $R_{k,l}$ for all channels k and recorded orientations l :

$$(67) \quad \hat{R}_{k,l} = \arg \max_r \mathcal{F}_m\{y_{k,l}[m]\} \left(\Omega = \frac{N_{fft} r}{R_{max}} \right)$$

The range estimate $\hat{R}_{k,l}$ is determined geometrically from the distances of each channel's transmit and receive antenna to the reflector. If the sensor is mounted to rotate in azimuth, the range depends on the rotation angle θ_l :

$$(68) \quad \hat{R}_{k,l} = \frac{\|\vec{r}_{TX,k} - \vec{r}_S(l)\| + \|\vec{r}_{RX,k} - \vec{r}_S(l)\|}{2}$$

$$(69) \quad \vec{r}_{TX,k} = \begin{bmatrix} x_{TX,k} \\ y_{TX,k} \\ \hat{\epsilon} \end{bmatrix}, \vec{r}_{RX,k} = \begin{bmatrix} x_{RX,k} \\ y_{RX,k} \\ \hat{\epsilon} \end{bmatrix},$$

$$(70) \quad \vec{r}_S(l) = \begin{bmatrix} (\hat{R}_S - \hat{\epsilon}) \sin(\hat{\theta}_S - \theta_l) \\ 0 \\ (\hat{R}_S - \hat{\epsilon}) \cos(\hat{\theta}_S - \theta_l) \end{bmatrix},$$

If the sensor is mounted to rotate in its elevation, the reflector appears to move depending on the rotation in elevation ϕ . For a given rotation angle ϕ_l , the reflector

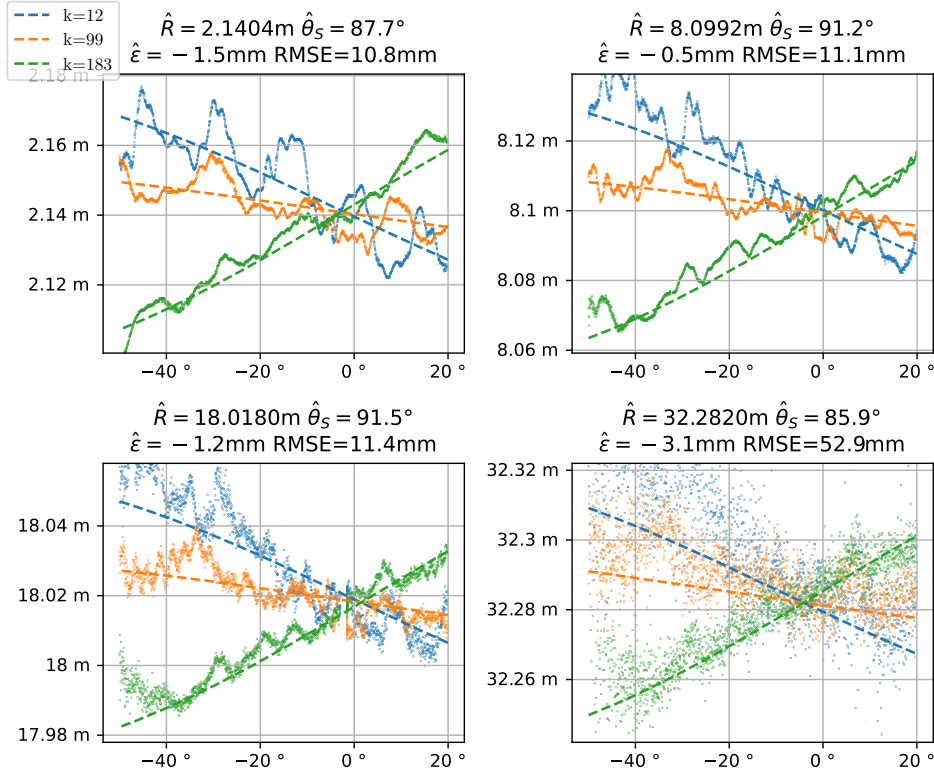


FIGURE 3.11. Example Optimization Results

is located at

$$(71) \quad \vec{r}_S(l) = \begin{bmatrix} 0 \\ (\hat{R}_S - \hat{\epsilon})\sin(\hat{\phi}_S - \phi_l) \\ (\hat{R}_S - \hat{\epsilon})\cos(\hat{\phi}_S - \phi_l) \end{bmatrix},$$

In our setup, a signal is recorded with θ (or ϕ , respectively) from 0° to 180° , with the reflector located at roughly $R_S = \{2, 8, 18, 32\}$ m and either $\theta_S = 90^\circ$ or $\phi_S = 90^\circ$.

With this, the loss \mathcal{L} can be defined as the mean square difference between \hat{R} and R_p , the mean being computed as the average over all K channels and L sensor rotations:

$$(72) \quad \mathcal{L}(\hat{R}_s, \hat{\theta}_s, \hat{\epsilon}) = \frac{1}{KL} \sum_{l=0}^{L-1} \sum_{k=0}^{K-1} (R_{k,l} - \hat{R}_{k,l}(\hat{R}_s, \hat{\theta}_s, \hat{\epsilon}))^2$$

Figure 3.11 shows the result of 100 iterations at an adaption rate of 0.05 at the example of three different channels, comparing the measured spectral peaks (shown as points) to the estimated position (dotted line) of the reflector. Only a subset of orientations is used for the estimate, namely $-50^\circ < \theta_l - 90^\circ < 20^\circ$.

For the first three measurements, the peak location oscillates around the estimate by 1 to 2 cm. The *root mean square error* (RMSE) is reduced to 11 mm. Due

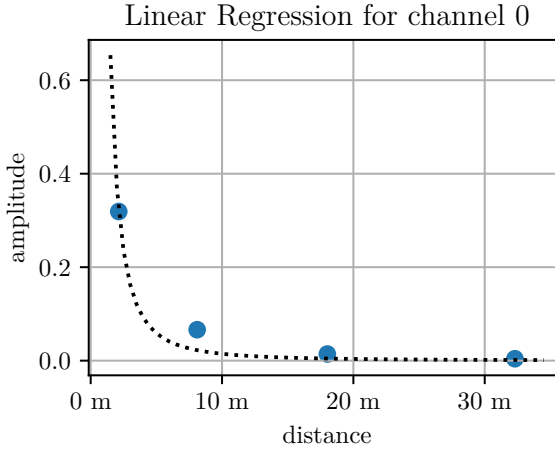


FIGURE 3.12. Example transmission coefficient Linear Regression

to the decreasing signal level received from higher distances, the fourth measurement has a higher relative noise level, resulting higher movement of the spectral peaks, and hence a much higher RMSE.

3.4. Amplitude. First, the recorded amplitudes are analyzed, beginning with the influence of the angle of arrival. To do this, each channel's range FFT spectrum's amplitude is evaluated at the respective calculated peak location $\hat{\Omega}$, and then normalized by dividing it by its maximum.

The first parameters to extract are the three real-valued factors A_i , B_j and $c(\theta, \phi)$. First, we define a quantity that will be referred to as the transmission coefficient:

$$(73) \quad \alpha_k = \sqrt{\frac{\sigma}{4\pi} A_i B_j}$$

Since the channel characteristic has been constrained to $[0, 1]$, the transmission constant can be expressed in terms of the two distances $R_1 = \|\vec{r}_s - \vec{r}_{Tx,k}\|$ and $R_2 = \|\vec{r}_s - \vec{r}_{Rx,k}\|$, and other known constants:

$$(74) \quad \max_{\theta, \phi} |C_k(R, \theta, \phi)| = \alpha_k \frac{\lambda}{4\pi R_1 R_2} = \alpha_k \frac{1}{R_1 R_2} \frac{2\pi c_0}{\omega}$$

$$(75) \quad = \alpha_k \frac{1}{4\pi R_1 R_2} \frac{2\pi c_0}{\omega_0 + \dot{\omega} \frac{R_1 + R_2}{c_0}}$$

$$(76) \quad = \alpha_k \frac{c_0^2}{2R_1 R_2 (\omega_0 c_0 + \dot{\omega}(R_1 + R_2))}$$

With that, an estimate of the transmission coefficient $\hat{\alpha}_k$ can be obtained via linear regression. An example linear regression is shown in Figure 3.12, and the resulting estimates with their standard deviations are summarized in Figure 3.13.

Having estimated the channel gains, we can now turn to analysing the channel characteristics. Assuming the optimal range bin $\hat{\Omega}$ is evaluated each time, we get

$$\left| \mathcal{F}_m\{y_k[m]\}(\Omega = \hat{\Omega}) \right| = |C_k(\vec{r})|$$

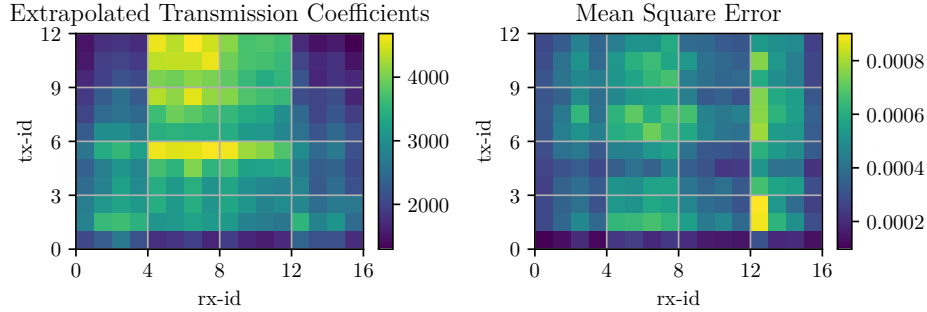


FIGURE 3.13. transmission coefficient Linear Regression Results

Dividing that by the maximum gain (76) yields

$$(77) \quad \frac{|C_k(\vec{r})|}{\max_{\theta,\phi} |C_k(R, \theta, \phi)|} = c_k(\theta, \phi)$$

Figure 3.14 provides an overview by displaying the mean channel characteristic for each measurement. It can be seen that the gain is strongest when the target is directly in boresight, tapering off when the target is off-center. The reduction in gain is stronger when the target moves off to the side in the elevation, than in azimuth. While the target remains stronger than background noise up until an azimuth angle of around -75° to 75° , it can only be seen in an elevation angle sector from -25° to 25° .

The graphs of the horizontal measurements appear slightly asymmetrical, an effect which is investigated in the following.

A possible explanation for the asymmetry is the sensor mount, which protrudes out on the right side of the array, attenuating the signal received by antennas on that side when the reflector is behind said protrusion [NEEDS DRAWING].

Investigating the individual channel gains (c.f. 3.15) gives a first indication: the asymmetry is most pronounced when comparing the range of 30° to 60° to its counterpart of -30° to -60° for the horizontal measurements. Namely, in the former range, the gain seems to oscillate every 16 channels.

To explore further, Figure 3.16 zooms in on one period. It shows the channel gain of the horizontal measurements for angles 30° to 60° of the channels in which transmit antenna 0 is active, arranged by the horizontal position of the receive antenna, from left to right. It can now be seen that the channel gain of antennas closer to the sensor mount's protrusion drops in amplitude at lower angles than that of the antennas further away from it, confirming that the sensor mount is responsible for the asymmetry. To get a more accurate estimate of the channel characteristics, the measurements have to be repeated with the sensor mounted on the outside.

With this, the individual antenna gains and the channel characteristics have been extracted from the data. In the next step, the recorded phases are analyzed.

3.5. Phase Estimation Techniques. The first step in extracting the phase parameters from the recorded data is yet again evaluating the signal's DFT phase

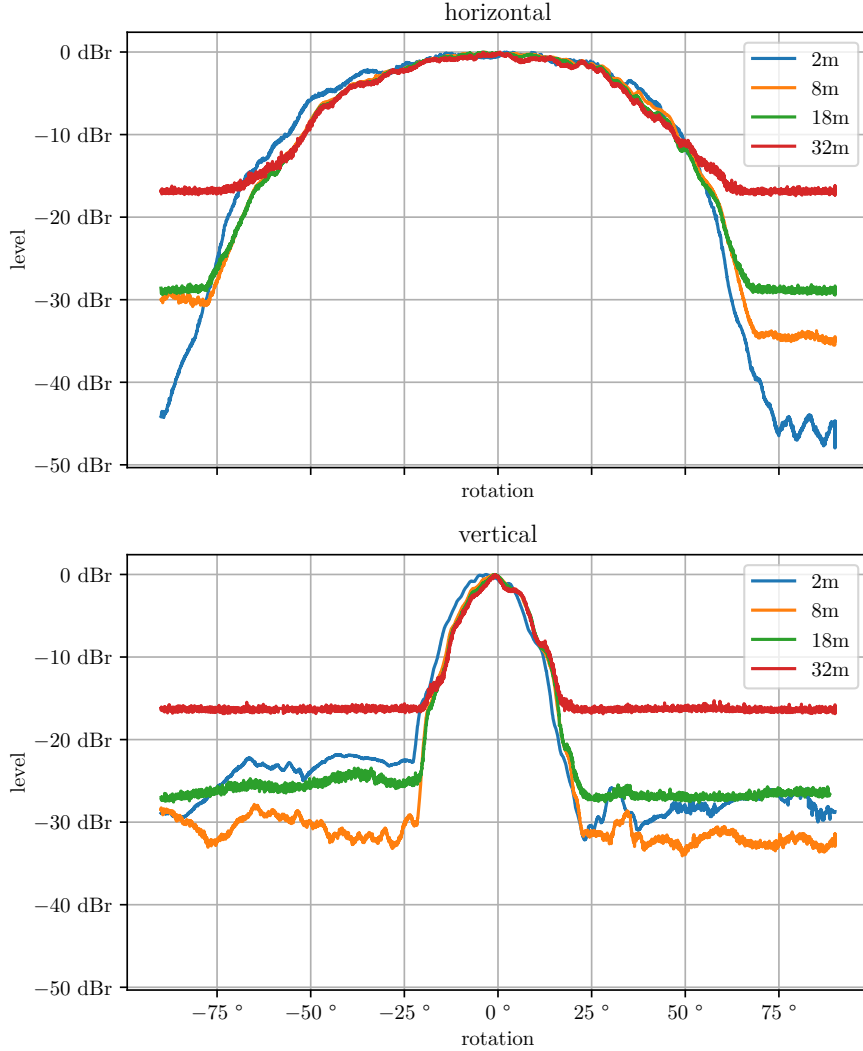


FIGURE 3.14. Mean Channel Characteristic for multiple reflector distances

at the optimum range bin $\hat{\Omega} = \frac{N\omega}{c_0 f_s} \hat{R}_k$, which according to (66) should ideally yield

$$(78) \quad \Phi_k(\vec{r}_S) := \arg \mathcal{F}_m\{y_k[m]\}(\hat{\Omega}(\vec{r}_S))$$

$$(79) \quad = \arg \underline{C}_k(\vec{r}_S)$$

$$(80) \quad = \omega_0 \tau_k(\vec{r}_S) + \varphi_k$$

$$(81) \quad \text{with } \varphi_k = \frac{\psi_i + \theta_j}{2} \text{ and } \tau_k = \frac{2R_k}{c_0}$$

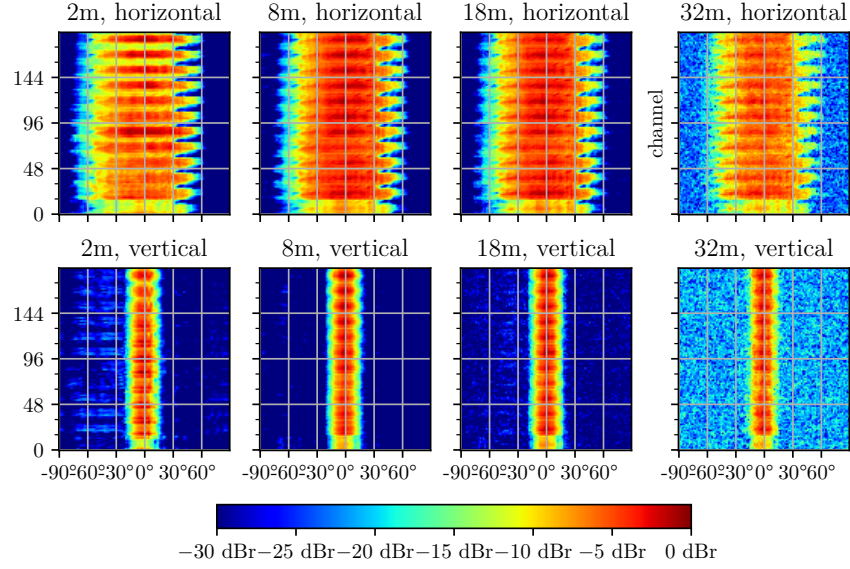


FIGURE 3.15. Channel-wise amplitude for multiple distances

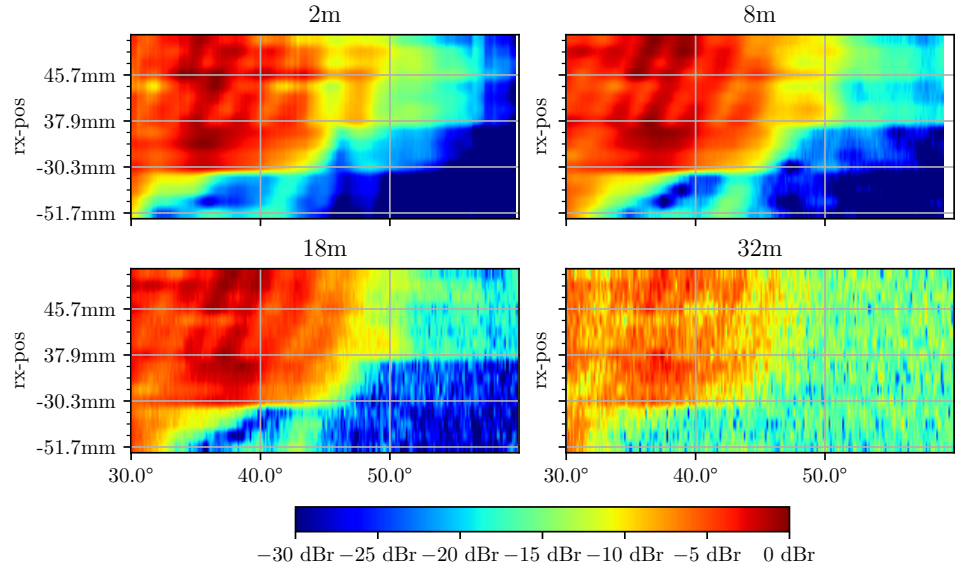


FIGURE 3.16. Channel-wise amplitude for multiple distances, channels arranged by Rx antenna position, only Tx antenna 0 active

However, this part of the analysis is highly dependent on the accuracy of our assumptions, specifically the distance between reflector and sensor. The phase $\Phi_k(\theta) = \omega_0 \frac{2R_k(\theta)}{c_0} + \varphi_k$ changes immensely with small changes in said distance.

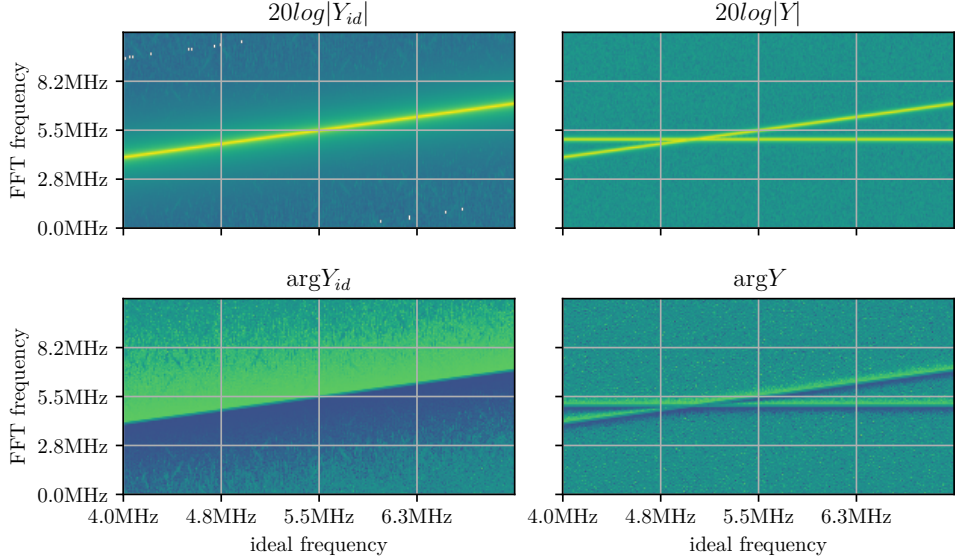


FIGURE 3.17. Spectra of example signal Y and Y_{id}

To illustrate, a change of $\Delta R_k = 1$ mm would cause approximately the following phase shift:

$$\begin{aligned}\Delta\Phi_k &= \omega_0 \frac{2\Delta R_k}{c_0} \\ &= 2\pi \cdot 77 \cdot 10^9 \text{ Hz} \cdot \frac{2 \cdot 1 \cdot 10^{-3} \text{ m}}{3 \cdot 10^8 \text{ m/s}} \\ &= 0.5133\pi = 92.4^\circ\end{aligned}$$

The range estimate made in subsection 3.3 had an RMSE of at least 11 mm, which introduces high uncertainty into the phase evaluation.

Another method to extract the phase from the recorded data is evaluating the FFT at the spectral peak, which was the method of choice in 2. Which method copes better with the presence of interference? In the following, we will illustrate the effects of interference with a simulated signal, as well as the impact of the interference on the two estimation methods accuracy.

Consider the signal received by an arbitrary channel of the array $y(t, \theta)$. Its frequency slowly changes as the orientation angle θ ; for simplicity's sake, let the frequency shift linearly with $\omega(\theta) = 2\pi(5 \text{ MHz} + 1 \text{ MHz} \cdot \theta), \theta \in [-1, +3]$. This results in our ideal signal

$$y_{id}(t = mT_s, \theta) = 1 \cdot e^{-j\omega(\theta)mT_s}$$

Introducing a source of interference with constant frequency ω_0 and the amplitude 0.1, as well as a gaussian noise source $n(t, \theta) \sim \mathcal{N}(0; 0.001)$, we get

$$y(t = mT_s, \theta) = 1 \cdot e^{-j\omega(\theta)mT_s} + 0.1 \cdot e^{-j\omega_0 mT_s} + n(t, \theta)$$

The spectrum of the ideal signal $Y_{id}(\Omega, \theta)$ and the degraded signal $Y(\Omega, \theta)$, calculated with an $N = 2048$ point FFT with $M = 512$ samples in long-time, each corresponding to a different angle θ , is shown in fig. 3.17 in amplitude and phase. The location of the both signals' spectral maxima can be seen in fig. 3.18a, showing that the interference causes the spectral maximum to move from its ideal location.

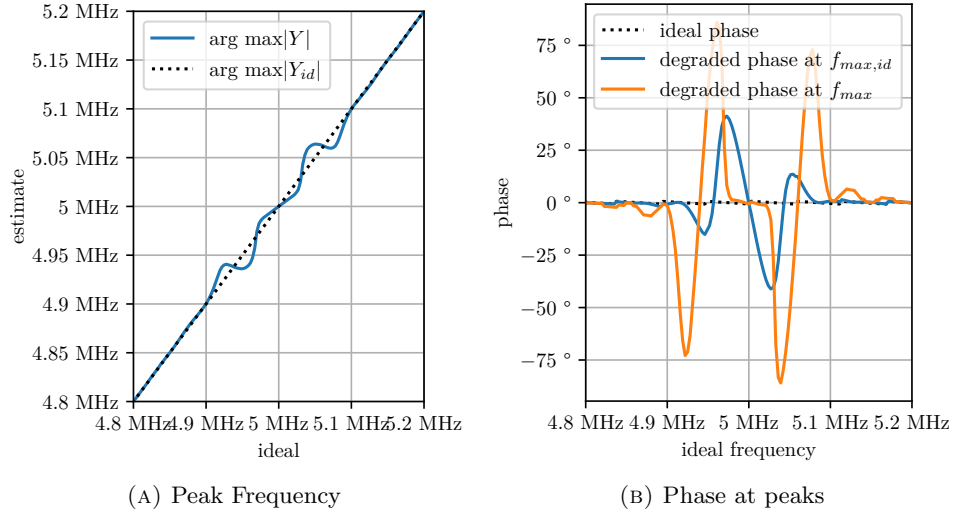
FIGURE 3.18. Extracting Phase from example spectra Y and Y_{id}

Figure 3.18b finally shows the effect of interference on the phase. We compare the phase of the ideal signal to phase of the degraded signal, which is evaluated at both the ideal and the degraded signal's spectral maxima. It can be seen that the latter method's phase diverges much more strongly from the ideal phase than that of the former, and should therefore be preferred in the subsequent analysis.

3.6. Phase Analysis. With knowledge of the robustness of our phase estimation against range estimation errors, the task of extracting the phase parameters can be continued. For better legibility of any graphs generated from the signal, the phase of any given channel will be unwrapped from its original domain of $\theta \in [-\pi + \theta_s, \pi + \theta_s]$ such that no discontinuities are visible when plotting phase against sensor orientation, while maintaining the original phase for $\theta = \theta_s$.

To assess the performance of the two techniques introduced in the previous section, Figure 3.19 shows how they each compare to the signal model¹ for a few selected channels. As it turns out, while being theoretically less robust against interference, the phase evaluated at the signal peak is much smoother and matches our signal model much more closely.

Now, the channel phase offsets ϕ_k can be estimated using linear regression. Figure 3.20 shows an example linear regression, and the resulting channel phase offsets are shown in Figure 3.21.

3.7. Antenna Separation. To describe the array in terms of its channel gains is somewhat redundant. As was defined in the underlying signal model, each channel gain $C_k e^{j\varphi_k}$ in actuality just the product of the transmit and receive antenna gains, that is

$$(82) \quad C_k^2 e^{j2\varphi_k} = A_i e^{j\psi_i} \cdot B_j e^{j\vartheta_j} \text{ for } k = N_{Tx} i + j$$

¹In this case, the signal model shown for comparison assumes that $\varphi_k = 0, \forall 0 \leq k < K$. Thus, the phase shown here is directly proportional to the estimated range \hat{R}_k :

$$\hat{\Phi}_k(\theta) = \omega_0 \tau_k + 0 = \frac{\omega_0}{c_0} 2\hat{R}_k(\theta).$$

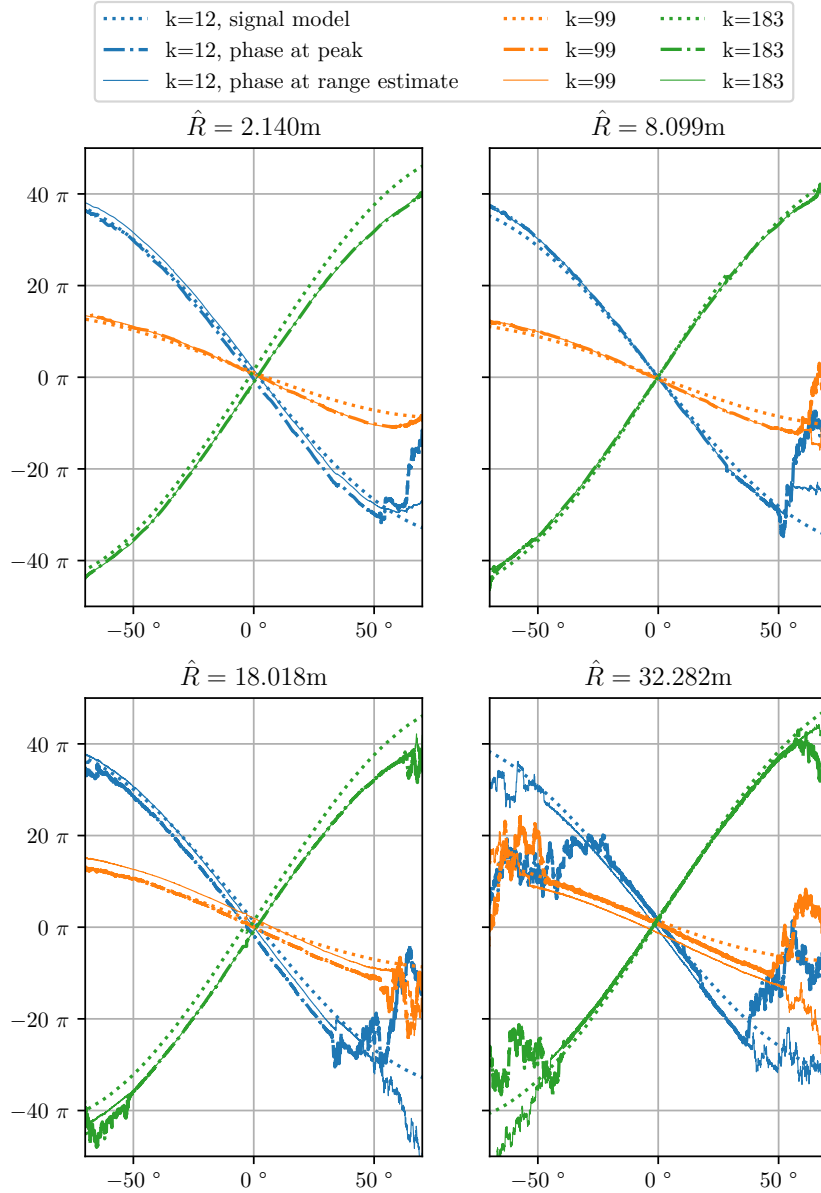


FIGURE 3.19. Extracted Phase from measured signal, compared to signal model

To more accurately describe the array, the next step in our analysis is to estimate antenna gains of the receive and transmit array. Multiple combinations were feasible, but the rightmost receive antenna 0 was defined as a reference antenna, such that $B_0 = 1$ and $\vartheta_0 = 0$.

In the following, the channel gain amplitudes \hat{C}_k that were estimated in subsection 3.4, and the channel phase offsets $\hat{\varphi}_k$ from subsection 3.6 are used to obtain

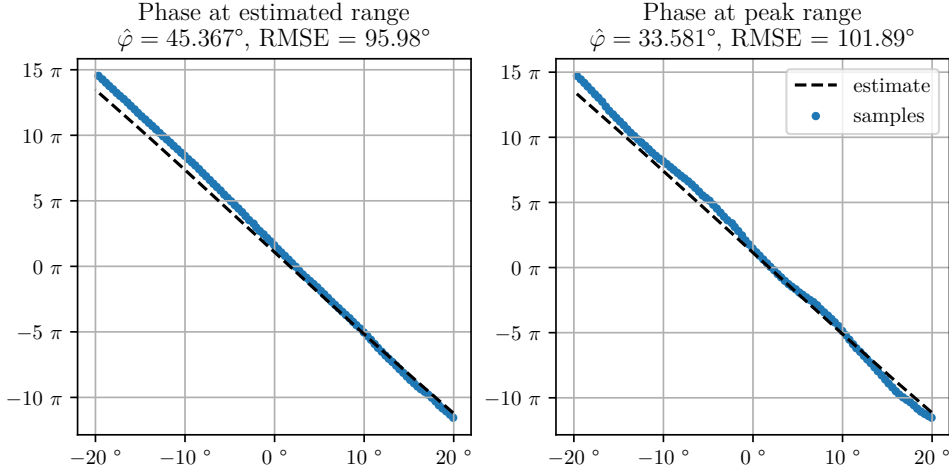


FIGURE 3.20. Example: Channel 12 Phase Linear Regression

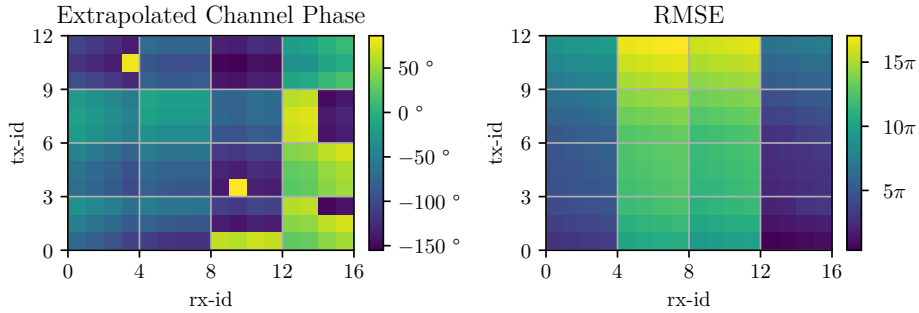


FIGURE 3.21. Phase Linear Regression Overview

estimates for the transmit and receive antenna parameters.

Thanks to the definition of a reference antenna, the transmit antennas' amplitude and phase are easily obtained:

$$(83) \quad \hat{A}_i = \hat{C}_k^2 \Big|_{k=N_{Tx}i}$$

$$(84) \quad \hat{\psi}_i = \hat{\varphi}_k \Big|_{k=N_{Tx}i}$$

With that, a least squares estimate for the remaining receive antennas' amplitude and phase is:

$$(85) \quad \hat{B}_{j \neq 0} = \frac{1}{N_{Tx}-1} \sum_{i=1}^{N_{Tx}-1} \frac{\hat{C}_k^2}{\hat{A}_i} \Big|_{k=N_{Tx}i},$$

$$(86) \quad \hat{\psi}_{j \neq 0} = \frac{1}{N_{Tx}-1} \sum_{i=1}^{N_{Tx}-1} \frac{2\hat{\varphi}_k}{\hat{\psi}_i} \Big|_{k=N_{Tx}i}$$

The resulting antenna parameters are shown in tables 2a and 2a.

Antenna	Gain	Phase	Antenna	Gain	Phase
0	$4.134 \cdot 10^6$	53.596°	0	1.000	0.000°
1	$7.847 \cdot 10^6$	125.805°	1	1.463	-7.095°
2	$7.363 \cdot 10^6$	48.354°	2	1.676	-26.095°
3	$6.169 \cdot 10^6$	-126.556°	3	1.426	0.712°
4	$5.445 \cdot 10^6$	-13.976°	4	3.797	-1.052°
5	$6.815 \cdot 10^6$	-111.434°	5	3.635	26.672°
6	$5.174 \cdot 10^6$	-81.855°	6	3.999	42.318°
7	$3.962 \cdot 10^6$	82.760°	7	3.703	-2.503°
8	$3.517 \cdot 10^6$	119.322°	8	3.391	49.492°
9	$2.831 \cdot 10^6$	1.485°	9	2.867	-2.698°
10	$2.291 \cdot 10^6$	7.703°	10	2.751	69.663°
11	$2.158 \cdot 10^6$	-53.846°	11	2.631	-40.625°
(A) Tx Antennas			12	1.393	8.481°
(B) Rx Antenna Gains			13	0.987	-11.289°
			14	1.129	-1.515°
			15	0.820	-5.109°

TABLE 2. Estimated Antenna Parameters with Reference Rx0

3.8. Conclusion. In this section, a method for estimating the antenna gains from real-world antenna measurements has been formulated that optimizes the estimation’s accuracy and robustness against interference. The summarized steps are as follows:

- (1) Setup the reflector in front of the sensor. For each distance to measure, center the reflector by observing a live readout of the phase at the spectral peak caused by the reflector, and positioning the sensor such that the phase differences between channels is minimal.
- (2) From the measurements, extract the range of the spectral peak caused by the reflector for each channel and sensor orientation. Use numerical optimization to find a set of model parameters (\hat{R}_s , $\hat{\theta}_s$ or $\hat{\phi}_s$, and $\hat{\epsilon}$) that best matches the spectral peaks.
- (3) Evaluate the amplitude of the spectrum at the frequency corresponding to the estimated range from the previous step. The maximum amplitude across all angles is the channel gain C_k/R^2 , and the remaining attenuation is the channel characteristic $\hat{c}_k(\theta, \phi) \in [0, 1]$. With linear regression across all measured distances, the channel gain at 1 m can be estimated. The estimated channel characteristic $\hat{c}_k(\theta, \phi)$ can indicate orientations with low SNR and/or high interference.
- (4) Evaluate the phase of the spectrum at the frequency corresponding to the estimated range. Unwrap the phase of each channel such that the phase for $\theta = \hat{\theta}_s$ is in $[-\pi, \pi]$. Find the channel phase offset φ_k that best matches the signal model to the measured phase.
- (5) Separate each square channel gain $\hat{C}_k^2 e^{j2\hat{\phi}_k}$ into a transmit gain $A_i e^{j\psi_i}$ and a receive gain $B_j e^{j\vartheta_j}$. Do this by defining a receive antenna as a reference.

Following these steps gives a decent estimate of the systems’s physical properties with relatively lax requirements on the measurement itself. This is especially desirable since section 2 demonstrated a need for frequent in-field calibration, since

the system parameters may change after restarting, and also shift over time.

More sophisticated methodology is required to achieve accurate measurements of the system. Controlling the positioning of the reflector relative to the sensor more closely, for example by placing the reflector on a linear axis, would greatly improve accuracy.

Interference sources in the environment would also have to be reduced. This would involve moving the experiment to a more controlled environment, such as a low-reflection room.

Another area of improvement lies in channel separation. Since the reference antenna in the described method is not external, but rather a part of the system under test, all the results of our analysis indicate are relative differences between antennas. Instead, an external antenna with known characteristics could replace the reflector, allowing for more accurate measurements of the individual antennas' absolute characteristics.

CHAPTER 4

Image Reconstruction

In the preceding chapter, a comprehensive analysis of the radar stability and antenna gain measurements, were conducted to understand the factors influencing system performance over time. Valuable insights into the temporal characteristics of the radar system were gained through this investigation, serving as the foundation for subsequent imaging experiments.

In this chapter, the focus shifts to radar imaging. Building upon the insights garnered from stability analysis and antenna gain measurements, three distinct imaging algorithms are implemented and evaluated using the PyTorch framework. These algorithms include an FFT-based approach, a Backprojection method, and a hybrid algorithm combining elements of both.

PyTorch is introduced in section 1 as a versatile tool for implementing radar processing algorithms. Following this, the implementation and evaluation of three distinct imaging algorithms is described: section 2 focuses on FFT-Based Imaging, where we explore the offline calibration, assess *Direction of Arrival* (DOA) accuracy, and present test images. In Section 3, we shift our attention to Back-projection Imaging, examining DOA accuracy and showcasing test images. Section 4 introduces the Hybrid Approach, where we evaluate DOA accuracy and present test images. Finally, Section 5 provides a comprehensive summary, comparing and analyzing the performance of the three algorithms to provide insights into their respective strengths and limitations.

1. PyTorch

The algorithms implemented in this chapter are presented in the PyTorch framework. As a machine learning framework, it provides accelerated tensor processing. Tensors, ie. rectangular multidimensional arrays are a perfect fit to describe the signals sent by the sensor and the subsequent signal processing.

Given that a significant portion of the operations in the imaging algorithms are parallelizable, considerable performance gains can be achieved with the built-in parallel processing of tensor operations in PyTorch. While parallel processing on a CPU already improves runtimes substantially, even better performance can be attained with GPU-enabled parallel processing, which is currently available using the CUDA-API on NVIDIA GPUs.

To aid in understanding any code listings referenced in this chapter, a brief tutorial is included in section 1 that discusses some key parts of PyTorch's syntax for tensor processing.

2. FFT-Based Imaging

The first imaging algorithm to be implemented is based on the FFT. A detailed description of the algorithm can be found in subsection 3.1, but the following is an abridged summary to reiterate the key principles.

The range is estimated by computing the FFT spectrum of each time signal; due to the FMCW principle, the frequency of the received signal is directly related

to its range. Then, making the assumption of planar incident waves as well as having calibrated the array to achieve coherence between channels, the angle of arrival can be estimated using FFTs over the ULA subset of the sensor's virtual antenna array. The resolution can be increased by zero-padding the signal before applying the FFT. An example implementation in PyTorch is shown in code listing B.1.

Here, the function `calc_image` returns a 3D-image of dimension $N_{range} \times N_{azimuth} \times N_{elevation}$. Its input consists of `data`, a time data tensor of dimension $M \times K$, the calibration weights `weights` of dimension K , and `settings`, a dictionary of settings. `settings` is expected to contain the input and output dimensions, the indices of the ULA subset of the virtual array with gaps indicated by -1 , as well as the window functions to be used in each FFT.

2.1. Direction of Arrival Accuracy. This section aims to illustrate the theoretical capabilities of FFT-based DoA-estimation on the iMCR. The directivity in azimuth and elevation is simulated for multiple distances to illustrate the impact of near-field conditions.

For this, the input time signal is an ideal point source (see eqn. 24), located at $(R, \theta = 0, \phi = 0)$ assuming a constant channel gain of $\underline{C}_k(r, 0, 0) = 1 \forall r, k$:

$$(87) \quad \underline{y}_k[m] = e^{-j\omega\tau_k m T_s}, \quad k \in [0, K - 1], m \in [0, M - 1]$$

The time of flight τ_k is computed using the physical measurements of the array. The image is computed for multiple distances at resolution $N_{range} = 1024$, $N_{azimuth} = 2048$ and $N_{elevation} = 8$, and evaluated at the range and evaluation bin of the scatterer. The resulting peaks in azimuth are shown in Figure 4.1.

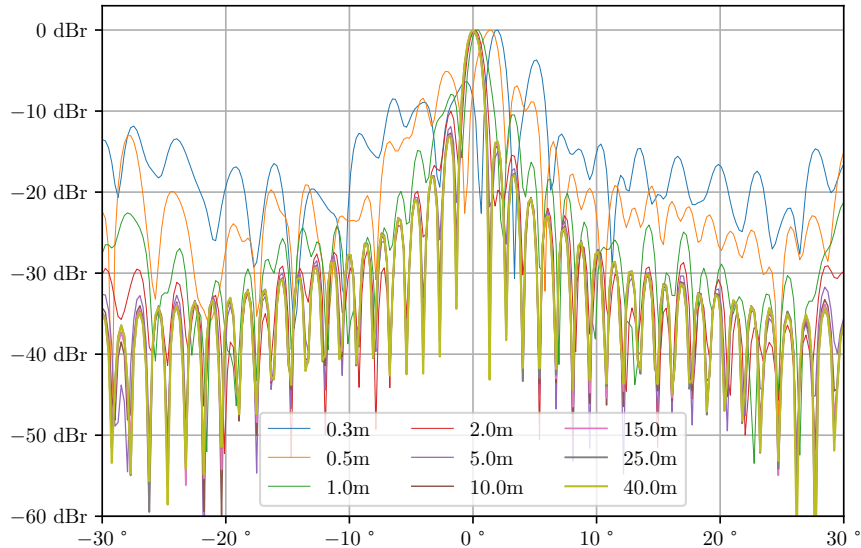


FIGURE 4.1. iMCR FFT direction of arrival estimation: theoretical accuracy in azimuth for an ideal point scatterer at different ranges

The Fraunhofer distance of the array can be computed from the wavelength $\lambda_0 = 3.944$ mm and the virtual array's azimuth aperture $D_{azm} = 86 \frac{\lambda_0}{2} = 16.96$ cm:

$$(88) \quad d_f = \frac{2D_{azm}}{\lambda_0} = 14.59 \text{ m}$$

It can be seen that for targets closer than d_f , the peak deteriorates in multiple ways. The location of the peak moves to higher angles than the actual location of $\theta = 0^\circ$. For targets at 30 cm, the peak has moved to $\theta = 2.02^\circ$.

In near-field conditions, the side lobe levels increase until their minimum only around 20 dB below the peak, whereas in the far field, the minimum is 60 dB below the peak.

In far-field conditions, the main peak at $\theta = 0^\circ$ is clearly separated from its sidelobes by pronounced local minima. The minimum to the right of the main peak starts to disappear below d_f , and the peak to the right starts to merge with the main peak the closer the target gets. The far-field half-power and quarter-power beamwidths are approximately $\theta_{3\text{dB}} = 1.9^\circ$ and $\theta_{6\text{dB}} = 2.6^\circ$, respectively.

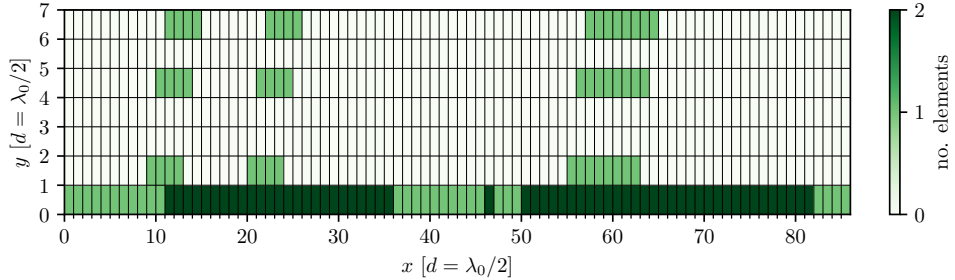


FIGURE 4.2. iMCR virtual antenna array occupancy

For direction of arrival estimation in azimuth, the 86-channel ULA subset of the array is well applicable to an FFT-based approach, even with its reduced performance in near-field conditions. Yet in elevation, such a ULA subset does not exist, as the array is sparse in elevation, both horizontally and vertically (c.f. 4.2): in most columns, only one virtual antenna is present.

To still use the FFT, a possible approach would be “backfilling” the array with zeros to obtain a complete uniformly spaced rectangular virtual array. The FFT is then computed over the columns (c.f. 4.2) of the resulting URA, each yielding a spectrum that is related to the direction of arrival in elevation.

A disadvantage of this approach is that it can cause substantial spectral leakage. Our backfilled array $b[k]$ is mathematically equivalent to applying a binary window function $w[k]$ to the ideal rectangular array $a[k]$:

$$\begin{aligned} b[k] &= w[k] \cdot a[k] \\ \text{e.g. } b[0..7] &= [b_0, b_1, 0, 0, b_2, 0, b_3, 0], \\ w[0..7] &= [1, 1, 0, 0, 1, 0, 1, 0], \\ \text{and } a[0..7] &= [a_0, a_1, a_2, \dots, a_7] \end{aligned}$$

However, this window function causes additional peaks to appear in the spectrum, since multiplication in the time domain is equivalent to convolution in the frequency domain:

$$\begin{aligned} \mathcal{F}\{b[k]\}[n] &= \mathcal{F}\{w[k] \cdot a[k]\}[n] \\ &= W[n] * A[n] \end{aligned}$$

In case of the example given above,

$$|W[0..7]| = [4.00, 0.77, 1.41, 1.85, 2.00, 1.85, 1.41, 0.77]$$

It would be possible to reduce the spectral leakage with deconvolution algorithms. To show the starting point for these algorithms, the unadulterated spectral peak for targets at multiple distances is shown in Figure 4.3.

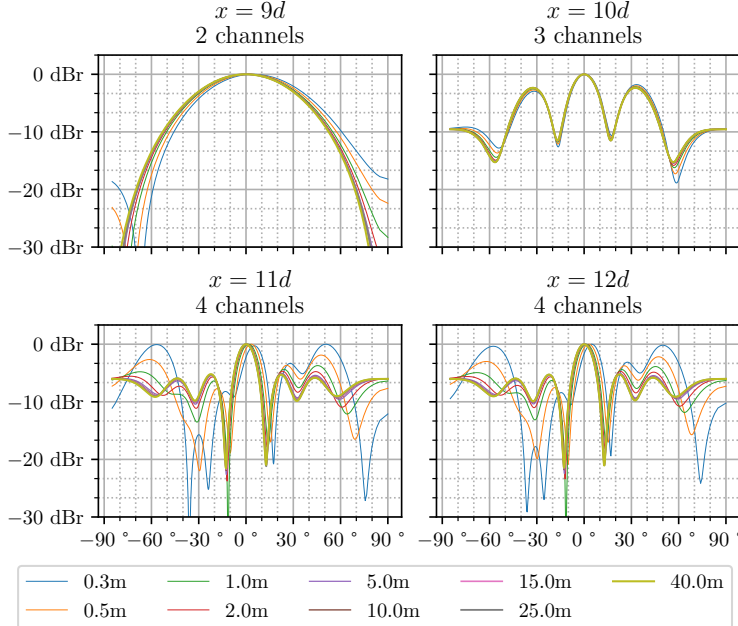


FIGURE 4.3. iMCR FFT-based direction of arrival: theoretical accuracy in elevation for an ideal point scatterer at different ranges and different array subsets

It can be seen that the half-power beamwidth improves the more channels are included in the sub-array: for two, three and four active channels, we approximately get $\phi_{3\text{dB}} = 60^\circ$, 14° and 12° , respectively.

As the peak narrows, the spectrum contains more and more sidelobes. For sub-arrays that include three channels, the side peaks are the strongest, barely 3 dB less than the main peak.

The Fraunhofer distance of the array in elevation can be computed from the wavelength $\lambda_0 = 3.944 \text{ mm}$ and the virtual array's maximal elevation aperture $D_{elv} = 7 \frac{\lambda_0}{2} = 1.38 \text{ cm}$:

$$(89) \quad d_f = \frac{2D_{elv}^2}{\lambda_0} = 9.66 \text{ cm}$$

The Fraunhofer distance in elevation is smaller than in azimuth by an order of magnitude. Thus, all distances considered lie in the far-field, and the shape of the peak should not change a lot over distance.

While this holds true for the two- and three-channel case, if four channels are considered, the shape does change with distance.

On the one hand, the location of the main peak moves to higher angles if the range is decreased. On the other hand, the first two sidelobes decrease in amplitude, while the third ones move towards $\phi = 0^\circ$ and increase in amplitude.

TODO:

- Change Code listing

2.2. Offline Calibration. To compute the angle of arrival, it is critical that the input signal be coherent in both amplitude and phase.

This is done by deviding each channel's range spectrum $Y_k(\Omega)$ by its corresponding estimate channel gain $\hat{C}_k e^{j\hat{\varphi}_k}$. As well as aligning the phases correctly, this also equalizes the channel gains. Note that this approach does not take the channel gain pattern into account, but only its static amplitude, since the same channel gain estimate is used for all directions.

2.3. Test Image. To give an indication how well the theoretical capabilities of the FFT-based approach translate into real world applications, a test scene was recorded. The sensor is placed facing the front of a building with circular walls, and a reflector is placed between them, slightly off-center at a distance of approximately 6 m.

The target 2D image spans a 24×15 m area in the horizontal plane, with square pixels of edge length 10 cm, and the sensor located on one of the image's long sides, namely $[x, y] = [0, 0]$.

It is constructed by first calculating the polar-coordinate FFT image at a resolution of $N_{range} \times N_{azimuth} = 2048 \times 512$. The image can then be extracted from by selecting the range- and azimuth bins m and k that correspond to each pixel $[x, y]$:

$$(90) \quad m = \left\lfloor N_{range} \frac{\sqrt{x^2 + y^2}}{R_{max}} \right\rfloor$$

$$(91) \quad k = \left\lfloor \frac{N_{azimuth}}{2} \left(\sin \arctan \left(\frac{y}{x} \right) + 1 \right) \right\rfloor$$

Figure 4.4 shows the resulting image with and without calibration. It can be seen that increases output SNR, which results in a higher contrast image. Also, the azimuth response improves, decreasing the width of the peak caused by the reflector. Furthermore, in the calibrated image, the outline of the tower is easier to make out. Altogether, the image still contains too many artifacts in azimuth: each peak of the image coincides with a semi-circle centered on the sensor. We have shown that this behaviour is expected in subsection 2.1: the theoretically achievable main lobe without windowing is about 40 dB higher than the others. To improve image clarity, a decrease in dynamic range through thresholding may be required.

3. Backprojection Imaging

The second imaging algorithm to be implemented is backprojection. A detailed description of the algorithm can be found in subsection 3.2, but the gist of it is the following:

Backprojection works by computing the correlation between the incoming time data and the signal of an isotropic scatterer (see Equation 24) at an arbitrary set of locations. The ideal signal for the isotropic scatterer at a given location \vec{r} is computed using the measured complex channel gains at that location $\hat{C}_k(\vec{r})$:

$$s_k[m] = \hat{C}_k(\vec{r}) e^{-j\hat{\omega}\tau_k(\vec{r})mT_s}$$

At this point, an intensity normalization in range could also be implemented simply multiplying the ideal signal with r^2 . The same is achievable in cross-range by inverting the amplitude of the channel gains.

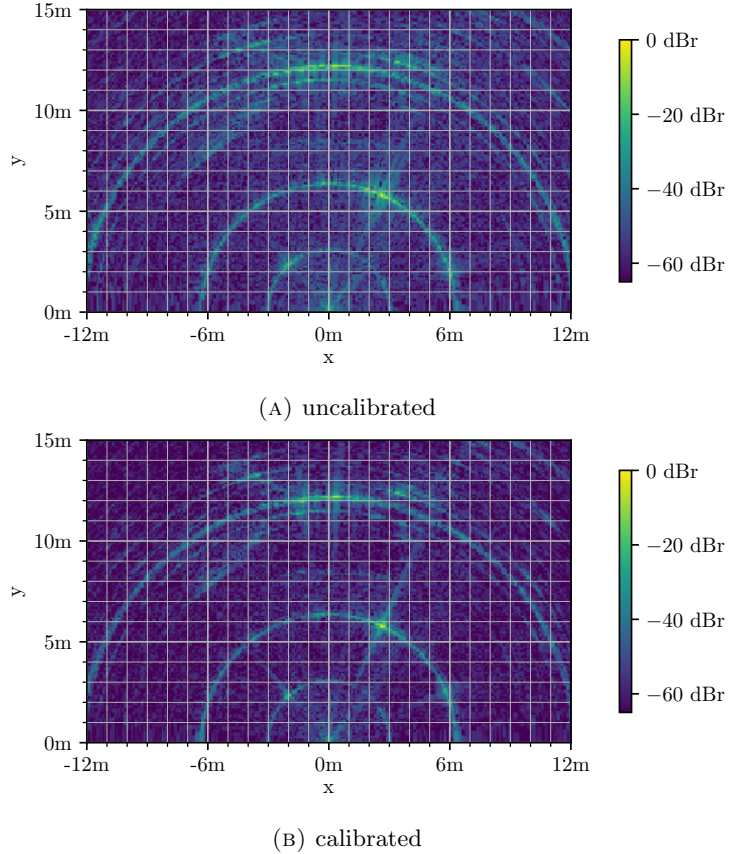


FIGURE 4.4. FFT-based image generated from real data

Since the channel gains are assumed to be static, the ideal signals can be pre-computed for generating images for at multiple points in the long-time dimension. An example implementation in PyTorch is shown in code listing B.3.

A major limitation implementations with pre-calculated weights is its scalability. Pre-calculating the weights, while allowing for decent opportunities in decreasing the runtime through parallel processing, quickly use a prohibitive amount of memory.

If there are Z individual locations, M sample points in time and K channels, then $M \cdot K \cdot Z$ weights need to be computed. For example, the weights for a uniformly spaced image with a rather low resolution of $Z = 100 \cdot 10 \cdot 100 = 100$ kilovoxels, at $K = 192$ and $M = 1022$, stored as complex numbers consisting of two 64 bit floating point numbers, would require

$$\begin{aligned} & M \cdot K \cdot Z \cdot 2 \cdot 64 \text{ bit} \\ & = 1022 \cdot 192 \cdot 10^5 \cdot 16 \text{ byte} \\ & = 3.14 \cdot 10^{12} \text{ byte} = 3.14 \text{ TB} \end{aligned}$$

of memory. With the projections of Moore's law [4], this amount of memory should be available in consumer-level computers by the year 2050. Until then, the memory requirements have to be reduced by re-computing the weights and applying them to the input data along an arbitrary dimension. For example, recomputing them

for every of the sampled time points would reduce the memory requirements by a factor of 1022 to a more manageable size of around 3 GB.

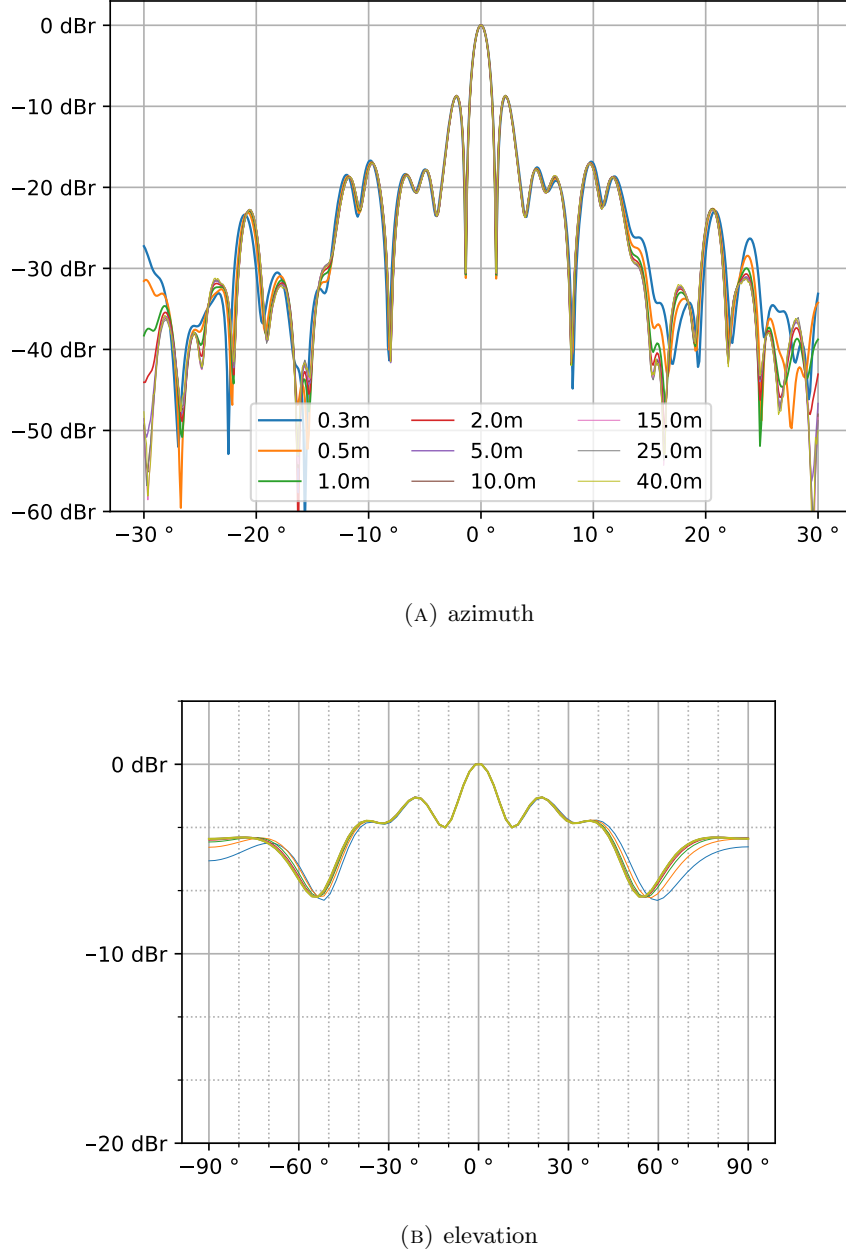


FIGURE 4.5. iMCR backprojection direction of arrival estimation: theoretical accuracy for an ideal point scatterer at different ranges

3.1. Direction of Arrival Accuracy. To better understand the DoA-estimation capabilities of the algorithm, the azimuth and elevation response is simulated for multiple distances to illustrate the impact of near-field conditions. The same input

signal as in subsection 2.1 is used.

The image is computed for multiple distances at resolution $N_{range} = 1$, $N_{azimuth} = 512$ and $N_{elevation} = 1$. Naturally, the range of the image is set to the range of the ideal target each time. The resulting peaks in azimuth and elevation are shown in figures 4.5a and 4.5b, respectively.

In both azimuth and elevation, it can be seen that the peak no longer deteriorates in what were near-field conditions for the FFT-based approach. The peak and most side lobes remain virtually identical across all considered ranges. Essentially, the backprojection algorithm has brought Fraunhofer distance closer in range, because the array is re-focused for every inspected point. In azimuth, the level of the sidelobes stabilizes at around 30 dB to 40 dB below the peak, whereas in elevation, the sidelobe level is merely 3 dB to 6 dB below the peak.

The azimuth half-power beamwidth is approximately $\theta_{3\text{ dB}} = 1.6^\circ$ and the azimuth quarter-power beamwidth approximately $\theta_{6\text{ dB}} = 2.4^\circ$. In elevation, the half-power beamwidth is approximately $\phi_{3\text{ dB}} = 20^\circ$ and the quarter-power beamwidth approximately $\phi_{6\text{ dB}} = 100^\circ$.

A possible way to increase directivity in elevation is to increase the elevation channels' impacts by applying higher weights to them. Since 13 of 16 Rx-antennas are located at the same height, their impact on the elevation response is disproportionately high.

- discuss windowing

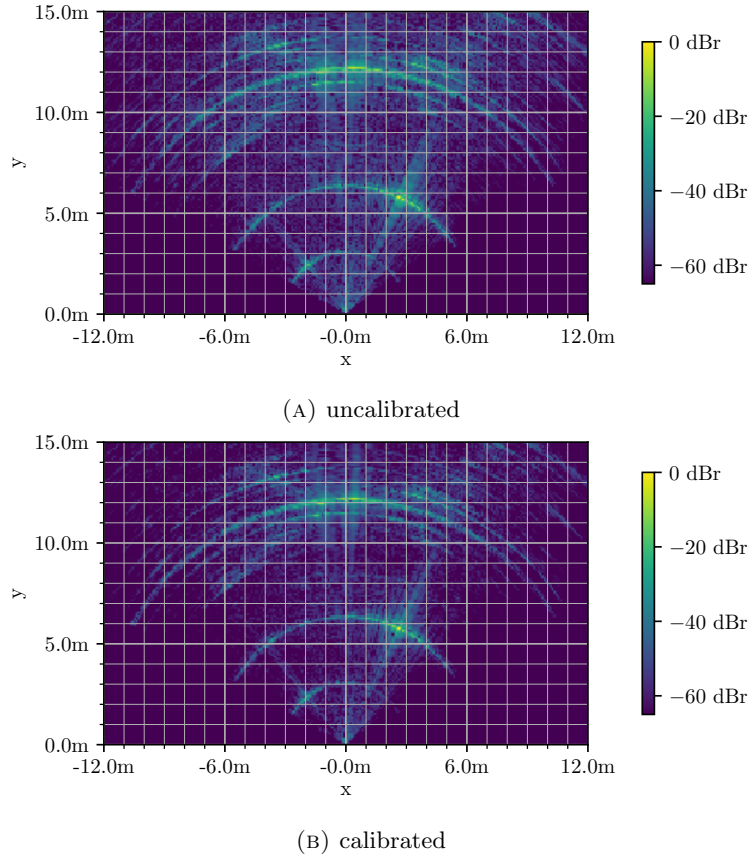


FIGURE 4.6. Backprojection image generated from real data

3.2. Test Image. The theoretical capabilities of the backprojection algorithm are again tested for real world applications, using the same scene as in subsection 2.3.

Once again, the target 2D image spans a 24×15 m area in the horizontal plane, with square pixels of edge length 10 cm, and the sensor located on one of the image's long sides, namely $[x, y] = [0, 0]$ m. Unlike the FFT-based approach, the backprojection algorithm allows for an arbitrary set of sample points, so no further transformations are required to obtain an image with square pixels.

In Figure 4.6, the resulting images obtained with and without calibration are compared. Calibration demonstrates several notable effects: Calibration leads to an enhanced SNR and a reduction in the width of azimuth peaks. Additionally, the influence of antenna gain patterns becomes apparent, causing attenuation in off-center regions and for longer distances. As predicted in the previous section, the direction of arrival estimation is not perfect, even for ideally calibrated data. Each peak is accompanied by a circular artifact at the same range, concentric to the sensor.

Compared to FFT imaging, the noise attenuation appears to have improved for both images. This expected, since the FFT-approach only uses 86 out of the 192 available channels, while backprojection uses all of them. This should lead to up to double the noise attenuation, as the following brief detour into estimation theory will explain.

Doubling the number of samples in the presence of any additive zero-mean noise can lead to a halving of the noise variance due to the properties of the sample mean estimator and the central limit theorem. The sample mean estimator is given by:

$$(92) \quad \hat{\mu} = \frac{1}{N} \sum_{i=1}^N x_i$$

where x_i are the individual samples and N is the number of samples. The variance of the sample mean estimator is given by:

$$(93) \quad \text{Var}(\hat{\mu}) = \frac{\sigma^2}{N}$$

where σ^2 is the variance of the noise.

As the number of samples N increases, the variance of the sample mean estimator decreases proportionally to $\frac{1}{N}$. Hence, doubling the number of samples effectively halves the noise variance, resulting in a more accurate estimate of the true value.

4. Hybrid Approach

Compared to the FFT-based approach, the backprojection algorithm is a lot more computationally intensive, taking multiple orders of magnitude longer to compute a single 2D image. The runtime of the implemented algorithm confirms the results from the complexity analysis in subsection 3.4: while the FFT-based approach has a complexity of $\mathcal{O}(MK \log MK)$, the backprojection approach costs $\mathcal{O}(ZMK)$.

As explained in subsection 3.2, it is possible to replace part of the computation with an inverse FFT, taking advantage of the increased speed and lower memory consumption of the inverse FFT-algorithm, while sacrificing some accuracy. An example implementation of the backprojection-FFT-hybrid algorithm can be found in B.6. Its theoretical performance is investigated in the next section. Afterwards, a test image is computed.

4.1. Direction of Arrival Accuracy. Due to the inherent frequency quantization of the FFT, this hybrid approach is prone to get inaccurate estimates of the actual backprojection of a channel. This mismatch between the actual frequency to analyse, and the closest sampled frequency in the computed FFT can be reduced by zero-padding the input signal to increase the sample density.

To better understand how the accuracy of DOA estimation is affected by this, the azimuth response is simulated for multiple input lengths. The same input signal as in subsection 2.1 is used, only this time, a single distance is evaluated. Figure 4.7 shows the result of this simulation.

It can be seen that the main lobe and the first two side lobes stay identical in shape. The rest of the azimuth response is more strongly affected by the spectral resolution. However, the level of the minor lobes stays more or less unchanged, confirming the feasibility of the hybrid approach.

4.2. Test Image. The theoretical capabilities of the hybrid approach are put under the same test as the two previous algorithms. Once again, the target 2D image spans a 24×15 m area in the horizontal plane, with square pixels of edge length 10 cm, and the sensor located on one of the image's long sides, namely $[x, y] = [0, 0]$ m.

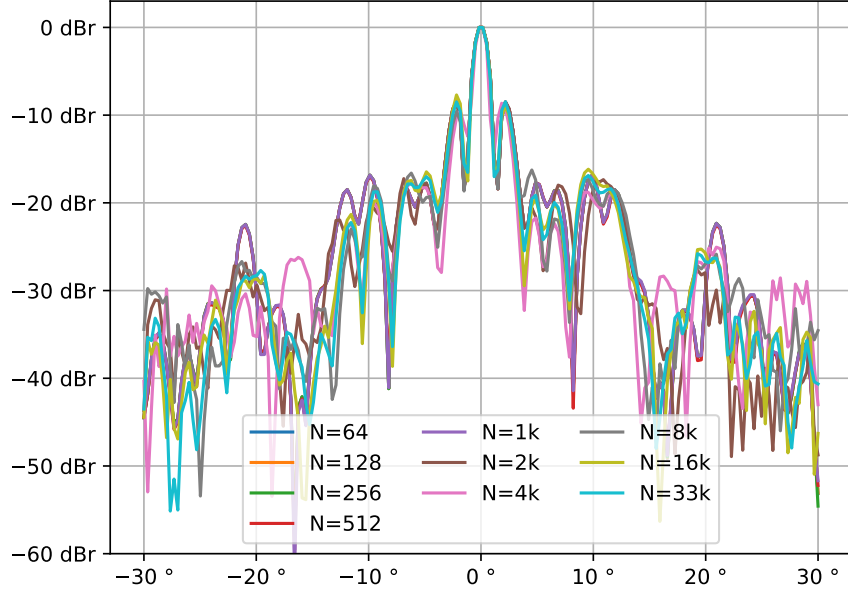


FIGURE 4.7. iMCR Backprojection-FFT-Hybrid direction of arrival estimation: theoretical accuracy in azimuth for an ideal point scatterer at different spectral resolutions

The resulting images looks very similar to those generated by the pure backprojection algorithm.

5. Conclusion

In this chapter, we embarked on a comprehensive exploration of radar imaging algorithms, evaluating their performance and efficacy in extracting meaningful information from radar data. Leveraging the insights gained from stability analysis and antenna gain measurements conducted in previous sections, we conducted a detailed examination of FFT-based imaging, Backprojection, and a hybrid approach. Through a systematic comparison of the resulting images and analysis of key metrics such as the azimuth and elevation peak widths, we gained a deeper understanding of the capabilities of each algorithm.

A comparison of the three implemented algorithms is given in Table 1. To start, the theoretically achievable half-power beamwidths are compared. In azimuth, the backprojection-based algorithm fair slightly better than the FFT, reaching 1.6° instead of 1.9° . In elevation, the approach for FFT-based DOA estimation can achieve a lower HPBW (12°) than backprojection (20°) if an appropriate vertical sub-array is selected. Note however that these vertical sub-arrays only consist of a maximum of four antennas, while the backprojection based DOA estimation always uses the entire array, resulting in a higher SNR. This effect is also seen in the SNR of the test images, where the backprojection approaches achieve an SNR of asdf for calibrated data, while the FFT only reaches asdf. For backprojection, a trade-off between the SNR improvement and the elevation HPBW can be made, where elevation channels are given greater weight in the calculation.

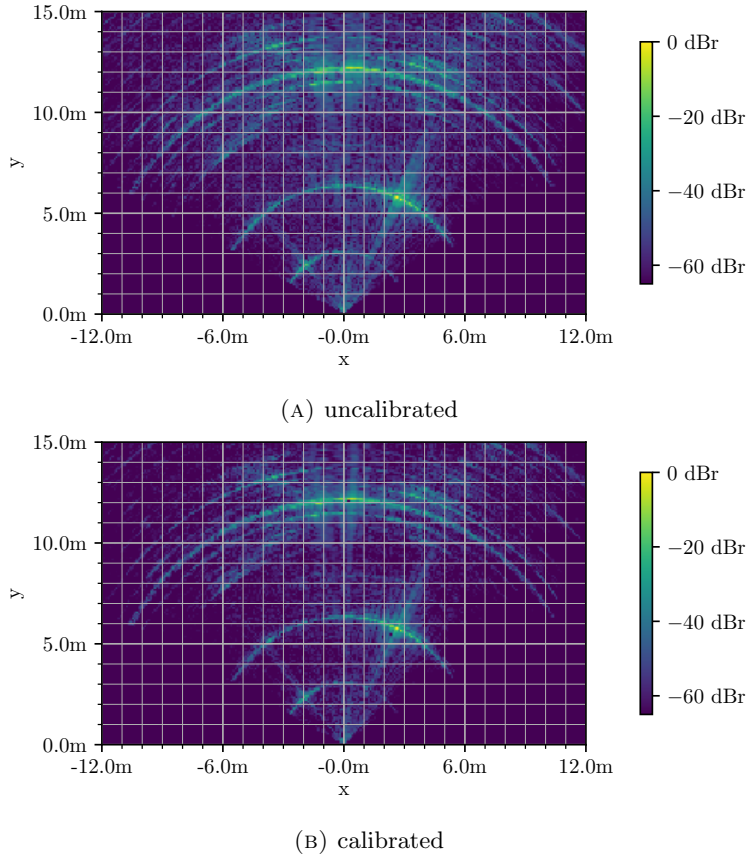


FIGURE 4.8. Backprojection-FFT-Hybrid image generated from real data

Another advantage of the backprojection algorithms is the reduced distortion in the near-field of the array, by essentially re-focusing it onto every point in the target image. One could argue that this reduces the Fraunhofer distance of the array to that of a single antenna with $D_{ant} = 7.6$ mm.

The obvious disadvantage of backprojection is its complexity and runtime. Even for a fairly low-resolution image, it takes around 70.87 s per frame, making it unfeasible for real-time applications. The hybrid approach works substantially better, achieving 95.9 ms per frame, suggesting the potential for real-time capabilities with further optimization. The FFT-based approach remains the fastest, averaging 1.4 ms per frame.

In conclusion, the backprojection offers significant potential for improvements in image fidelity over the FFT-approach. The near-field degradation of the DOA estimation is resolved and the potential SNR was increased. It offers arbitrary flexibility in the image's shape, a more robust DOA estimation in elevation and the application of measured antenna gains. While pure backprojection has prohibitively high runtimes, the hybrid approach demonstrates comparable performance to the FFT, suggesting potential for real-time capability with some optimization.

Further research is required to understand how the algorithm's performance can be enhanced by non-uniformly weighing the input data. In the FFT-based approach, a regular window function could be used to enhance the shape of the peak in range and reduce its side-lobe level. DOA-estimation could also be improved,

	FFT	Backprojection	Hybrid
HPBW, azimuth	1.9°	1.6°	1.6°
HPBW, elevation	12° to 60°	20°	20°
Fraunhofer Distance	14.50 m	30.4 mm	30.4 mm
complexity	$\mathcal{O}(MK \log MK)$	$\mathcal{O}(ZM^2K)$	$\mathcal{O}(K(Z + M \log M))$
test image runtime ¹	1.4 ms	70.87 s	95.9 ms
test image SNR			
input	ULA or URA	any	any
output	spherical	any	any

TABLE 1. Comparison between the three implemented algorithms

especially in elevation, by sacrificing some SNR gain for an enhanced HBPW by optimizing the weights for diversity.

CHAPTER 5

Conclusion and Discussion

In this final chapter, we reflect on the journey undertaken throughout this thesis, drawing together the threads of our research and exploring their broader significance. From the initial exploration of radar imaging algorithms to the in-depth analysis of their performance, each step has brought us closer to a deeper understanding of radar technology and its applications.

1. Overview

Chapter 1 of this thesis delineated two overarching objectives aimed at advancing radar imaging technology. Firstly, it sought to identify and evaluate a novel imaging algorithm capable of surpassing the limitations inherent in the current FFT-based approach developed for the system under test. Specifically, the chapter aspired to develop an algorithm harnessing measured antenna gains to enhance imaging precision and fidelity significantly. Secondly, the introduction provided a comprehensive overview of radar technology's pivotal role, particularly within the domain of mining applications. Through elucidating radar's pivotal role in streamlining bulk logistics and bolstering security measures, the chapter underscored the multifaceted applications of radar technology. These advancements hold promise for transformative applications across remote sensing, autonomous vehicles, and surveillance.

In chapter 2, foundational concepts essential for radar technology and imaging algorithms were explored. The chapter began with Antenna Fundamentals, introducing key parameters. It then provided a detailed framework in the Signal Model section, laying the groundwork for understanding signal processing in FMCW MIMO radar imaging and setting the stage for discussions on imaging algorithms, including the versatile Backprojection technique.

The hardware evaluation in chapter 3 delved into the meticulous examination of the iMCR sensor, assessing its stability and performance under various conditions. Through systematic measurements and analysis, the chapter provided valuable insights into the reliability and functionality of the hardware components, as well as the applicability of the proposed imaging algorithms.

Embarking on a comprehensive exploration of radar imaging algorithms in chapter 4, we evaluated their performance and efficacy in extracting meaningful information from radar data. Leveraging the insights gained from stability analysis and antenna gain measurements conducted in previous sections, a detailed examination of FFT-based imaging, Backprojection, and a hybrid approach was conducted. Through a systematic comparison of the resulting images and analysis of key metrics such as the azimuth and elevation peak widths, a deeper understanding of the capabilities of each algorithm was obtained.

2. Key Findings

This section encapsulates the pivotal discoveries extracted from both the hardware evaluation and imaging exploration. In Chapter 3, the thesis rigorously examines the stability and antenna characteristics of the radar hardware, uncovering fundamental insights crucial for radar imaging. These insights are complemented by the findings from Chapter 4, which delve into the performance and efficacy of various radar imaging algorithms.

The stability analysis of the radar system revealed consistent performance over time, with gradual changes observed in system parameters such as temperature and runtime. Frequent recalibrations were identified as essential for maintaining optimal system performance.

Antenna gain measurements provided valuable insights into the signal model's accuracy, confirming the feasibility of extracting antenna characteristics even from imperfect measurements.

Putting the imaging algorithms to the test revealed that, while the FFT-based approach offers the fastest runtime, Backprojection shows promising potential for improved image fidelity, particularly in reducing distortion in the near-field and enhancing signal-to-noise ratio (SNR). Furthermore, the hybrid approach demonstrates comparable performance to the FFT, suggesting real-time capability with further optimization. These results underscore the importance of selecting the appropriate imaging algorithm based on specific application requirements, balancing considerations such as runtime efficiency and image quality.

3. Outlook and Discussion

Concluding our investigation into real-time capable calibration and image reconstruction techniques for FMCW MIMO radars, it's essential to reflect on the significant insights garnered and explore avenues for future research. In this section, we discuss the implications of our findings, potential areas for improvement, and outline future directions in the field.

Exploring the stability of our experimental setup reveals subtle yet impactful influences on radar performance. Minor variations in temperature and humidity levels cause nuanced shifts within the system, gradually affecting measurement accuracy over time. Minimizing these environmental dynamics is crucial for better understanding the systems stability.

Further investigation into self-calibration mechanisms within the radar frontend would also improve our understanding of system stability. While designed to maintain system integrity, the inner workings of self-calibration remain somewhat opaque. Clarifying its duration, mechanisms, and effectiveness is an essential next step.

Temperature regulation emerges as another critical consideration for the stability measurements. Exploring controlled cooling measures, such as strategic cooler spray application, promises to highlight temperature-induced distortions in radar measurements. By observing corresponding changes in phase stability, researchers can develop robust temperature compensation strategies, ensuring consistent radar performance across diverse environments.

In antenna gain measurements, integrating an external reference antenna holds promise for enhancing measurement accuracy and precision. This approach enables absolute measurements, elevating the reliability of antenna characterization processes.

Meanwhile, exploring different radome configurations offers insights into fine-tuning antenna performance, vital for optimizing performance in dynamic environmental conditions.

Shifting focus to imaging algorithms, bridging the conceptual gap between FFT-based imaging and backprojection techniques presents exciting opportunities. Adapting windowing concepts from FFT-based imaging to backprojection could enhance image accuracy and fidelity. Also, to enhance the DOA capabilities of the backprojection algorithm, the array's diversity can be improved through appropriate windowing.

Implementing adaptive sampling techniques in image reconstruction offers promise for optimizing computational resources and enhancing real-time imaging capabilities. Regions of interest can be identified from low-resolution images, making it possible to adaptively increase the resolution only where it matters.

In summary, proposed improvements in stability analysis, antenna gain measurements, and imaging algorithms represent significant strides in improving imaging for FMCW MIMO radar systems. By embracing a culture of continuous improvement and fostering curiosity-driven research, researchers are poised to propel radar technology forward, driving incremental advancements that collectively revolutionize radar applications across diverse domains.

APPENDIX A

Bibliography

- [1] J. W. Cooley and J. W. Tukey, "An algorithm for the machine calculation of complex Fourier series," en, *Math. Comp.*, vol. 19, no. 90, pp. 297–301, 1965, ISSN: 0025-5718, 1088-6842. DOI: 10.1090/S0025-5718-1965-0178586-1. [Online]. Available: <https://www.ams.org/mcom/1965-19-090/S0025-5718-1965-0178586-1/> (visited on 02/29/2024).
- [2] R. Schmidt, "Multiple emitter location and signal parameter estimation," *IEEE Transactions on Antennas and Propagation*, vol. 34, no. 3, pp. 276–280, Mar. 1986, Conference Name: IEEE Transactions on Antennas and Propagation, ISSN: 1558-2221. DOI: 10.1109/TAP.1986.1143830.
- [3] C. A. Balanis, *Engineering Electromagnetics*, en. Wiley, May 1989, ISBN: 978-0-471-62194-2.
- [4] G. E. Moore, "Cramming more components onto integrated circuits, Reprinted from Electronics, volume 38, number 8, April 19, 1965, pp.114 ff.," *IEEE Solid-State Circuits Society Newsletter*, vol. 11, no. 3, pp. 33–35, Sep. 2006, Conference Name: IEEE Solid-State Circuits Society Newsletter, ISSN: 1098-4232. DOI: 10.1109/N-SSC.2006.4785860. [Online]. Available: <https://ieeexplore.ieee.org/document/4785860> (visited on 03/02/2024).
- [5] M. A. Richards, J. Scheer, and W. A. Holm, *Principles of Modern Radar*, en. SciTech Pub., 2010, ISBN: 978-1-891121-52-4.
- [6] A. Haderer, P. Scherz, C. Pfeffer, and A. Stelzer, "Real-time implementation of an imaging algorithm for FMCW MIMO radar systems," in *2012 9th European Radar Conference*, Oct. 2012, pp. 186–189.
- [7] "IEEE Standard for Definitions of Terms for Antennas," *IEEE Std 145-2013 (Revision of IEEE Std 145-1993)*, Mar. 2014, Conference Name: IEEE Std 145-2013 (Revision of IEEE Std 145-1993). DOI: 10.1109/IEEESTD.2014.6758443. [Online]. Available: <https://ieeexplore.ieee.org/document/6758443> (visited on 02/29/2024).
- [8] C. A. Balanis, *Antenna Theory: Analysis and Design*, en. John Wiley & Sons, Feb. 2016, ISBN: 978-1-118-64206-1.
- [9] M. Jankiraman, *FMCW Radar Design*, en. Artech House, 2018, ISBN: 978-1-63081-567-7.

APPENDIX B

Code

1. Introduction to PyTorch Sensor Processing

Pytorch Tensors can be created from python lists, or with a utility function like `zeros()`, `ones()` or `full()`:

```
1 >>> import torch
2 >>> torch.tensor(list(range(2)))
3 tensor([0, 1])
4 >>> torch.ones((2,3))
5 tensor([[1., 1., 1.],
6         [1., 1., 1.]])
```

Python's basic binary operators, such as `+`, `-`, `*` or `/`, can be used to operate on tensors. If both tensors are the same size, the operation is done element by element, similar to the hadamard product of matrices. Scalars can also be applied to tensors.

```
1 >>> torch.tensor(list(range(2))) + torch.ones(2)
2 tensor([1., 2.])
3 >>> 5 + torch.zeros(2)
4 tensor([5., 5.])
```

These operations are also allowed for tensors of different size, if their shapes follow the requirement that “[...] iterating over the dimension sizes, starting at the trailing dimension, the dimension sizes must either be equal, one of them is 1, or one of them does not exist.”¹

¹see <https://pytorch.org/docs/stable/notes/broadcasting.html>

For example, a $3 \times 2 \times 1$ tensor and a 1×2 tensor are broadcastable:

```

1 >>> a = torch.tensor([[[0],[1]],[[2],[3]],[[4],[5]]])
2 >>> b = torch.tensor([[1,10]])
3 >>> a.shape, b.shape
4 (torch.Size([3, 2, 1]), torch.Size([1, 2]))
5 >>> a+b
6 tensor([[[ 1, 10],
7           [ 2, 11]],
8
9           [[ 3, 12],
10          [ 4, 13]],
11
12          [[ 5, 14],
13          [ 6, 15]])]
14

```

In the third dimension, the elements of tensor **a** are broadcast onto the elements of tensor **b**. In the second dimension, the inverse is the case. The resulting tensor has the shape $3 \times 2 \times 2$.

Tensor indexing of one-dimensional tensors is identical to list indexing in python; and multi-dimensional tensors are indexed with a tuple of indices or slices. For example, to select all first elements of the previous result's third dimension, the following syntax is used:

```

1 >>> c=a+b
2 >>> c[:, :, 0]
3 tensor([[1, 2],
4         [3, 4],
5         [5, 6]])

```

Dimensions where a single index was used are omitted from the result. It is also possible to insert dimensions with the keyword **None**:

```

1 >>> c[:, :, 0].shape
2 torch.Size([3, 2])
3 >>> c[:, None, :, 0].shape
4 torch.Size([3, 1, 2])

```

Besides these basic operations, a plethora of functions is already implemented for tensors. Often, for each function operating on a tensor, there is also an equivalent member function of the class **tensor** that does the same. This makes composing functions a lot easier, because no nested parentheses are required:

```

1 >>> a = torch.randn((1,100))
2 >>> 20*torch.log10(torch.abs(torch.mean(a)))
3 tensor(-16.3953)
4 >>> 20*a.mean().abs().log10()
5 tensor(-16.3953)

```

2. Listings

```

1 def calc_image_fft(data, calibration, settings):
2     # range fft
3     W,N = settings['range_window'], settings['range_fftlen']
4     range_data = window_fft(data,W,N,0)
5     range_data /= calibration[None,:,:] # apply calibration
6
7     # azimuth fft
8     idx,W,N = settings['azm_ula'], settings['azm_window'], settings['azm_fftlen']
9     azimuth = window_fft(range_data[:,idx],W,N,1)
10
11    # elevation ffts
12    idx,W = settings['elv_ula'], settings['elv_window']
13    M,N,L = settings['range_fftlen'], settings['elv_fftlen'], idx.shape[-1]
14    elevation = torch.empty((M,N,L), dtype=torch.cfloat)
15    for l in range(L):
16        elevation[:, :, l] = window_fft(range_data[:, idx[:, l]], W, N, 1)
17
18    # estimate elevation gain
19    elevation_est = elevation.abs().mean(-1)
20    elevation_est /= elevation_est.max()
21
22    # return 3d image
23    img_3d = azimuth[:, :, None] * elevation_est[:, None, :]
24    return img_3d

```

LISTING B.1. PyTorch implementation of the FFT-based imaging algorithm

```

1 def window_fft(x, window, fftlen, dim):
2     fft = torch.fft.fft(x.transpose(dim,-1)*window, fftlen)
3     fft = torch.fft.fftshift(fft)/window.sum()
4     return fft.transpose(dim,-1)

```

LISTING B.2. PyTorch computation of a normalized FFT spectrum using a window function

```

1 def calc_image_bp(data, settings, pos):
2     M,K,L = data.shape
3     PP = pos.shape
4
5     gain = settings['channel gain']                      # PP x K
6     slope = settings['chirp slope']
7     f0 = settings['start frequency']
8     Ts = settings['sample period']
9
10    # Compute weights
11    tau = time_of_flight(settings, pos).unsqueeze(-2)    # PP x 1 x K
12    t = Ts*torch.arange(M)[:,None]                         # M x 1
13
14    freq = 2*torch.pi*slope*tau
15    phase = 2*torch.pi*f0*tau
16    weights = gain.unsqueeze(-2) * \
17        torch.exp(1j*freq*t) * \
18        torch.exp(1j*phase)  # PP x M x K
19
20    # Compute 3D Images
21    imgs = torch.empty((PP,L), dtype=torch.cfloat)
22    for l in range(L):
23        imgs[:,l] = (weights.conj() * data[:, :, l]).mean((-2,-1))
24    return imgs

```

LISTING B.3. PyTorch implementation of the backprojection imaging algorithm

```

1 def time_of_flight(settings, pos):
2     x_tx, x_rx = settings['x_tx'], settings['x_rx']
3     y_tx, y_rx = settings['y_tx'], settings['y_rx']
4     K=len(x_tx)
5     c0 = settings['lightspeed']
6
7     txpos = torch.tensor([x_tx,y_tx,[0]*K]).transpose(0,1)
8     rxpos = torch.tensor([x_rx,y_rx,[0]*K]).transpose(0,1)
9     # K x 3
10    pos = pos.unsqueeze(-2)
11    # PP x 1 x 3
12    r_tx = (txpos-pos).square().sum(-1).sqrt()
13    r_rx = (rxpos-pos).square().sum(-1).sqrt()
14    # sum(PPx1x3 - Kx3, -1) = PPxK
15    return (r_tx+r_rx)/c0

```

LISTING B.4. PyTorch computation of the channel-wise time of flight for a given position

```

1 def calc_pos(settings):
2     if settings['coordinate type'] == 'cartesian':
3         x0,x1,y0,y1,z0,z1 = settings['limits']
4         X,Y,Z = settings['resolution']
5         x = torch.linspace(x0,x1,X)[:,None,None].expand(-1,Y,Z)
6         y = torch.linspace(y0,y1,Y)[None,:,:None].expand(X,-1,Z)
7         z = torch.linspace(z0,z1,Z)[None,None,:].expand(X,Y,-1)
8     elif settings['coordinate type'] == 'cylindrical':
9         r0,r1,theta0,theta1,z0,z1 = settings['limits']
10        R,Theta,Z = settings['resolution']
11        r = torch.linspace(r0,r1,R)
12        theta = torch.linspace(theta0,theta1,Theta)
13        x = (r[:,None,None] * theta.cos() [None,:,:None]).expand(-1,-1,Z)
14        y = (r[:,None,None] * theta.sin() [None,:,:None]).expand(-1,-1,Z)
15        z = torch.linspace(z0,z1,Z)[None,None,:].expand(R,Theta,-1)
16    elif settings['coordinate type'] == 'spherical':
17        r0,r1,theta0,theta1,phi0,phi1 = settings['limits']
18        R,Theta,Phi = settings['resolution']
19        r = torch.linspace(r0,r1,R)
20        theta = torch.linspace(theta0,theta1,Theta)
21        phi = torch.linspace(phi0,phi1,Phi)
22        x = r[:,None,None] * theta[:,None,:,None].cos() * phi[None,None,:,:].sin()
23        y = r[:,None,None] * theta[:,None,:,None].sin() * phi[None,None,:,:].sin()
24        z = (r[:,None,None] * phi[None,:,None].cos()).expand(-1,Theta,-1)
25
26    return torch.stack((x,y,z),-1)

```

LISTING B.5. PyTorch computation of uniformly spaced sample positions in different coordinate systems

```

1 import torch
2
3 def calc_image_hybrid(data, settings, pos):
4     M,K = data.shape
5     PP = pos.shape[:-1]
6
7     gain = settings['channel gain']                      # P1xP2x...Pn x K
8     slope = settings['chirp slope']                     # P1xP2x...Pn x K
9     f0 = settings['start frequency']                   # P1xP2x...Pn x K
10    c0 = settings['lightspeed']                        # P1xP2x...Pn x K
11    Ts = settings['sample period']                    # P1xP2x...Pn x K
12    N = settings['ffflen']                            # P1xP2x...Pn x K
13    maxdist = c0/Ts / (4*slope)
14
15    fft = torch.fft.fft(data, n=N, dim=0)              # N x K
16    tau = time_of_flight(pos)                          # P1xP2x...Pn x K
17    weights = gain * torch.exp(2j*torch.pi*slope*tau) # P1xP2x...Pn x K
18    m_refl = (c0*tau/2 * N/maxdist).round().int()    # P1xP2x...Pn x K
19    phase = torch.exp(2j*torch.pi*f0*tau)             # P1xP2x...Pn x K
20
21    fft_flat = fft.flatten(0,-2)                      # N x K
22    img = torch.zeros(PP, dtype=torch.cfloat)          # P1xP2x...Pn x K
23    for k in range(K):
24        m_refl_flat = m_refl.flatten(0)[:,k]           # P1xP2x...Pn x K
25        fft_sel = fft_flat[m_refl_flat,k].unflatten(0,PP) # P1xP2x...Pn x K
26        img += weights.conj()*fft_sel / K
27
28    return img

```

LISTING B.6. PyTorch implementation of the FFT-backprojection hybrid algorithm

APPENDIX C

Additional Experiments

List of Figures

2.1 (a) Masking of a weak target response at $\hat{f} = 0$ by the sidelobes of a 30 dB stronger response at $\hat{f} = 0.2$. (b) Same two responses with Hamming window applied before the DTFT. Image and caption from [5, p.510]	12
3.1 The iMCR Sensor. closed housing (left) and open housing (right)	18
3.2 iMCR transmit and receive antenna positions	19
3.3 iMCR virtual array	20
3.4 Measurement Setup	21
3.5 Time Evolution of the Radar System's Temperature	22
3.6 Mean Intensity Spectrum	22
3.7 Change in reflector distance as measured by iMCR	23
3.8 Recorded drift over night	24
3.9 Drift by Antenna	25
3.10 Recorded drift and temperature with system restart	26
3.11 Example Optimization Results	29
3.12 Example transmission coefficient Linear Regression	30
3.13 transmission coefficient Linear Regression Results	31
3.14 Mean Channel Characteristic for multiple reflector distances	32
3.15 Channel-wise amplitude for multiple distances	33
3.16 Channel-wise amplitude for multiple distances, channels arranged by Rx antenna position, only Tx antenna 0 active	33
3.17 Spectra of example signal Y and Y_{id}	34
3.18 Extracting Phase from example spectra Y and Y_{id}	35
3.19 Extracted Phase from measured signal, compared to signal model	36
3.20 Example: Channel 12 Phase Linear Regression	37
3.21 Phase Linear Regression Overview	37
4.1 iMCR FFT direction of arrival estimation: theoretical accuracy in azimuth for an ideal point scatterer at different ranges	42
4.2 iMCR virtual antenna array occupancy	43
4.3 iMCR FFT-based direction of arrival: theoretical accuracy in elevation for an ideal point scatterer at different ranges and different array subsets	44
4.4 FFT-based image generated from real data	46
4.5 iMCR backprojection direction of arrival estimation: theoretical accuracy for an ideal point scatterer at different ranges	47
4.6 Backprojection image generated from real data	49

4.7 iMCR Backprojection-FFT-Hybrid direction of arrival estimation: theoretical accuracy in azimuth for an ideal point scatterer at different spectral resolutions	51
4.8 Backprojection-FFT-Hybrid image generated from real data	52

List of Tables

1	iMCR: Technical Overview	18
2	Estimated Antenna Parameters with Reference Rx0	38
1	Comparison between the three implemented algorithms	53